PHYSICAL REVIEW B **86**, 184422 (2012)

Structural and magnetic properties of isovalently substituted multiferroic $BiFeO_3$: Insights from Raman spectroscopy

Johan Bielecki,[1,*] Peter Svedlindh,[2] Dessie T. Tibebu,[3] Shengzhen Cai,[3] Sten-G. Eriksson,[3]
Lars Börjesson,[1] and Christopher S. Knee[3]
[1]*Department of Applied Physics, Chalmers University of Technology, SE-41296 Göteborg, Sweden*
[2]*Department of Engineering Sciences, Uppsala University, Box 534, SE-751 21 Uppsala, Sweden*
[3]*Department of Chemical and Biological Engineering, Chalmers University of Technology, SE-412 96 Göteborg, Sweden*

(Received 3 July 2012; revised manuscript received 11 October 2012; published 19 November 2012)

Raman spectra, supplemented by powder x-ray diffraction and magnetization data of isovalently A- and B-site substituted $BiFeO_3$ in the $Bi_{1-x}La_xFeO_3$ ($0 \leqslant x \leqslant 1$), $Bi_{1-x}Tb_xFeO_3$ ($0 \leqslant x \leqslant 0.2$), and $Bi_{0.9}Sm_{0.1}Fe_{1-x}Mn_xO_3$ ($0 \leqslant x \leqslant 0.3$) series, are presented. A good agreement between the structural transitions observed by x-ray diffraction and the vibrational modes observed in the Raman spectra is found over the whole substitutional ranges, and in particular we find spectroscopic signatures of a $PbZrO_3$-type structure for $Bi_{0.8}La_{0.2}FeO_3$. Mode assignments in the substituted materials are made based on Raman spectra of the end-members $BiFeO_3$ and $LaFeO_3$. Moreover, by comparing spectra from all samples with $R3c$ structure, the phonon assignment in $BiFeO_3$ is revisited. A close connection between the degree of octahedral tilt and the Raman shift of the A_1 oxygen $a^-a^-a^-$ tilt mode is established. An explanation for the strong second-order scattering observed in $Bi_{1-x}La_xFeO_3$ and $Bi_{1-x}Tb_xFeO_3$ is suggested, including the assignment of the previously mysterious $BiFeO_3$ mode at 620 cm^{-1}. Finally, the magnetization data indicates a transition from a cycloidal modulated state towards a canted antiferromagnet with increasing A-site substitution, while $Bi_{0.9}Sm_{0.1}Fe_{1-x}Mn_xO_3$ with $x = 0$ and 0.15 exhibit an anomalous closing of the hysteresis loop at low temperatures. For low A-site substitution levels ($x \leqslant 0.1$) the decreasing Raman intensity of the Fe derived modes correlates with the partial destruction of the spin cycloid as the substitution level increases.

DOI: 10.1103/PhysRevB.86.184422 PACS number(s): 77.80.−e, 78.30.−j, 61.05.cp, 75.50.Ee

I. INTRODUCTION

The discovery of the unusual coincidence of ordered magnetic and electric phases, that is, multiferroicity, at room temperature in the perovskite compound $BiFeO_3$, together with an observed magnetoelectric coupling in thin films,[1] have garnered plenty of scientific interest.[2–4] However, despite the promising properties $BiFeO_3$ is often associated with problematic impurities and compositional instabilities.[2] A potential route for alleviating these problems is isovalent atomic substitution on the Bi and/or Fe sites. This has the possibility to induce an increase in both the compositional stability as well as reducing the relatively large leakage current in $BiFeO_3$.[5,6] In addition, isovalent substitution can destroy the spin cycloid that prohibits a macroscopic first-order magnetoelectric coupling.[7]

The parent compound $BiFeO_3$ crystallizes in a perovskite $R3c$ structure that differs from the ideal cubic structure by a translational offset along [111] of the Bi cation and an antiphase tilt of the oxygen octahedra along all three directions ($a^-a^-a^-$ in Glazer notation[8]). Concurrent with the Bi offset is an activation of the Bi lone pair along the [111] direction and the resulting polarization gives rise to the ferroelectric properties of $BiFeO_3$.[9] The magnetic moments of the Fe^{3+} ions are arranged in a cycloidal fashion of periodicity 620 Å along [110], superimposed on a slightly canted G-type antiferromagnetic order.[10] In the absence of cycloidal spin order, as is achieved both in $BiFeO_3$ thin films[1] and isovalently substituted $BiFe_{1-x}Mn_xO_3$,[7] linear magnetoelectric effects in the noncentrosymmetric phases of $BiFeO_3$ related ceramics become symmetry allowed and activate by a coupling between the A-site ferroelectric translation and the B-site magnetization via the antiferrodistortive $a^-a^-a^-$ tilt of the oxygen octahedra.[11] Although the linear magnetoelectric effect is symmetry forbidden on a macroscopic scale, the Dzyaloshinskii-Moriya mechanism can still be used locally in bulk $BiFeO_3$ to achieve an electric switching of the spin cycloid.[12]

Upon isovalent substitution on the A site, disorder is introduced which eventually leads to a decoherence of the Bi lone pair and a concurrent change in space group from the polar $R3c$ to a nonpolar space group. The route from the polar to the nonpolar symmetries depends greatly on which substituting element is used, both in relation to its concentration and ionic size. La substitution is a particularly interesting case as the small change in ionic size from 116 to 117 pm between La^{3+} and Bi^{3+} (Refs. 2,13, and 14) makes dilution of the lone pair the main effect of substitution. Increasing the ionic size difference, as for example with Tb^{3+} (ionic radius 104 pm) or Sm^{3+} (ionic radius 108 pm), will also introduce significant lattice distortions as a direct consequence. The effects of isovalent A-site substitution has recently been investigated in several reports, both with neutron and x-ray diffraction (XRD) as well as electron microscopy investigations. Upon substituting the A site with the significantly smaller Tb, neutron diffraction shows a single transition from $R3c$ to the $GdFeO_3$-type $Pnma$ structure (tilt system $a^+b^-b^-$) starting at 15% Tb content, including a two-phase region between $x = 0.15$ and 0.175.[15] A similar transition, albeit more complicated, is reported in the intensely studied $Bi_{1-x}La_xFeO_3$ series.[5,16–19] Here the similar ionic radii between Bi and La makes it possible to stabilize several intermediate structures before the final $Pnma$ structure is reached at 50% La content.[16] XRD and electron diffraction (ED) data indicated a stabilized $R3c$ structure up to 20%

La content where a transition towards a *Pnma* structure of the $GdFeO_3$ type occurred.[17] However, a more recent study, also employing a combination of synchrotron XRD and ED, reported a total of four structural phases.[16] A single phase $R3c$ structure was reported up to $x = 0.1$, followed by a mixed phase region for $x < 0.18$. At this point, a single phase *Pnam* structure of the $PbZrO_3$ type was observed. A very slight increase in substitution to $x = 0.19$ resulted in a possibly incommensurate structure that was retained up to $x = 0.3$. Finally, the $GdFeO_3$ type *Pnma* structure was reached above $x = 0.5$.[16] These subtle structural transitions were further corroborated by neutron diffraction experiments where the $PbZrO_3$ structure with *Pbam* symmetry was observed for $Bi_{0.82}La_{0.18}FeO_3$. Signs of an incommensurate structure with diffraction peaks very similar to *Pbam* was, however, not observed until $x = 0.25$.[19] The *Pnam* and *Pbam* structures appear very similar from x-ray and neutron diffraction and the *Pnam* structure has only been identified by spatially local electron diffraction measurements.[16] Even though $PbZrO_3$ crystallizes in the *Pbam* structure,[20] we will use $PbZrO_3$ type to denote either *Pnam* or *Pbam*; this point will be discussed further in Sec. V C.

Apart from isovalent substitution on the *A* site, there is also the possibility of isovalent substitution on the *B* site. This introduces yet another source of structural distortion as well as the possibility of stabilizing enhanced ferromagnetic and magnetoelectric couplings.[7] Recent high resolution neutron diffraction data on the $Bi_{0.9}Sm_{0.1}Fe_{1-x}Mn_xO_3$ series show a transition towards the centrosymmetric orthorhombic *Imma* symmetry (tilt system $a^0b^-b^-$) starting at $x = 0.15$ and complete for $x = 0.3$.[21] However, Khomchenko *et al.* have shown a more complicated transition from a $R3c$ structure to an incommensurate structure via *Pnam* of the $PbZrO_3$ type.[22]

Motivated by the discrepancies in reported structural data as well as a general lack of detailed Raman studies, we present here Raman, powder x-ray diffraction (PXRD), and magnetization data on $Bi_{1-x}La_xFeO_3$ (Lax) ($0 \leqslant x \leqslant 1$), $Bi_{1-x}Tb_xFeO_3$ (Tbx) ($0 \leqslant x \leqslant 0.2$), and $Bi_{0.9}Sm_{0.1}Fe_{1-x}Mn_xO_3$ (Sm10Mnx) ($0 \leqslant x \leqslant 0.3$). The Raman spectra of the end-members $BiFeO_3$[23–33] (BFO) and $LaFeO_3$[34,35] (LFO) have been investigated previously in great detail and are used here as starting points when analyzing the spectra of the *A*-site substituted materials. To our knowledge, Raman spectra on $Bi_{1-x}Tb_xFeO_3$ and $Bi_{0.9}Sm_{0.1}Fe_{1-x}Mn_xO_3$ have not been published before, while $Bi_{1-x}La_xFeO_3$ has only been investigated to some extent with this technique.[17,36]

The reported Raman spectra of $Bi_{1-x}La_xFeO_3$ are in fact difficult to reconcile with the aforementioned diffraction data, as they have been interpreted as showing $R3c$ symmetry up to 20% La content and broadened *Pnma* spectra above.[17,36] Here we alleviate the discrepancies between Raman and diffraction experiments and show Raman spectra corresponding to a single $R3c$ phase for $x \leqslant 0.1$, *Pnma* for $x \geqslant 0.5$, a $PbZrO_3$-type structure for $0.175 \leqslant x \leqslant 0.4$, and a mixed $R3c$-$PbZrO_3$ phase for $x = 0.15$.

Similarly, both the $Bi_{1-x}Tb_xFeO_3$ and $Bi_{0.9}Sm_{0.1}Fe_{1-x}Mn_xO_3$ spectra show a gradual transition from $R3c$ to *Pnma* and *Imma*, respectively, in excellent agreement with the neutron diffraction studies.[15,21] For $Bi_{1-x}Tb_xFeO_3$, the transition is complete at $x = 0.2$, with a gradual nature at intermediate substitution levels being a sign of micron-scale substitution inhomogeneities.

Comparisons across the substitutional series are made which facilitates mode assignments and a detailed analysis of both the first- and second-order scattering. In particular, such a comparison within the $R3c$ phase gives us unique insights into the controversial phonon assignment of $BiFeO_3$.

The paper is structured as follows: In Sec. III the x-ray diffraction data are presented. This is followed by a detailed presentation of the Raman spectroscopy results of each individual substitution series in Sec. IV. Furthermore, Sec. V contains a discussion of the Raman results, where the different series are compared to each other. In addition, this section contains an extensive discussion on the strong second-order Raman scattering. Finally, the magnetization results are presented in Sec. VI.

II. EXPERIMENT

Samples for the Raman investigations of $Bi_{1-x}Tb_xFeO_3$, ($0 \leqslant x \leqslant 0.2$) and $Bi_{1-x}La_xFeO_3$ ($0 \leqslant x \leqslant 0.5$) families were synthesized utilizing a coprecipitation solution route starting from the nitrates of bismuth, the lanthanides, and iron to provide a precursor that revealed signs of perovskite formation after the initial 500 °C heat treatment. Further heatings of 2 h duration at increments of 50 °C up to the final sintering temperature of 850 °C were utilized with accompanying regrinds after each step. For the $Bi_{0.9}Sm_{0.1}Fe_{1-x}Mn_xO_3$ series $x = 0.0$, 0.15, and 0.30, and the $Bi_{1-x}Tb_xFeO_3$ samples $x = 0.05$, 0.10, 0.15, and 0.20 used in the present magnetization investigations, the samples were those of the original neutron diffraction studies and these were prepared via conventional solid state synthesis route as detailed elsewhere.[15,21] Raman spectra collected on equivalent samples prepared by the different synthesis routes showed good agreement, however, the solution route samples showed greater phase purity and larger particle size and were therefore preferred for the detailed Raman studies.

Powder x-ray diffraction (PXRD) measurements were carried out RT using a Bruker AXS D8 ADVANCE VARIO powder diffractometer (Cu$K\alpha_1 = 1.5406$ Å). The data were analyzed by the Rietveld method[37] using the GSAS program[38] to assess phase purity and the crystal structures of the materials. Scans presented herein (see Fig. 1) were collected in the 2θ range 15°–100°, with a step size of 0.0092° and 3.9 s collection time per step.

Raman spectra were collected with an DILOR XY-800 spectrometer. A single grating 300 mm focal distance configuration was used for low resolution spectra in the 130–1700 cm^{-1} range. For higher resolutions and spectral range 50–700 cm^{-1} a double subtractive 800 mm focal distance configuration was used instead. Different dispersion in the two grating configurations give rise to apparent differences in relative intensities when comparing the two kinds of spectra. The 514 nm line of an Ar^+ laser, focused through a long working distance 40× microscope objective, was used as excitation source. The laser power was held below 1 mW distributed over a laser spot with radius 2 μm. All spectra were taken with linear polarized light impinging on the sample and unpolarized light collected at the CCD. Due to substitution induced broadening

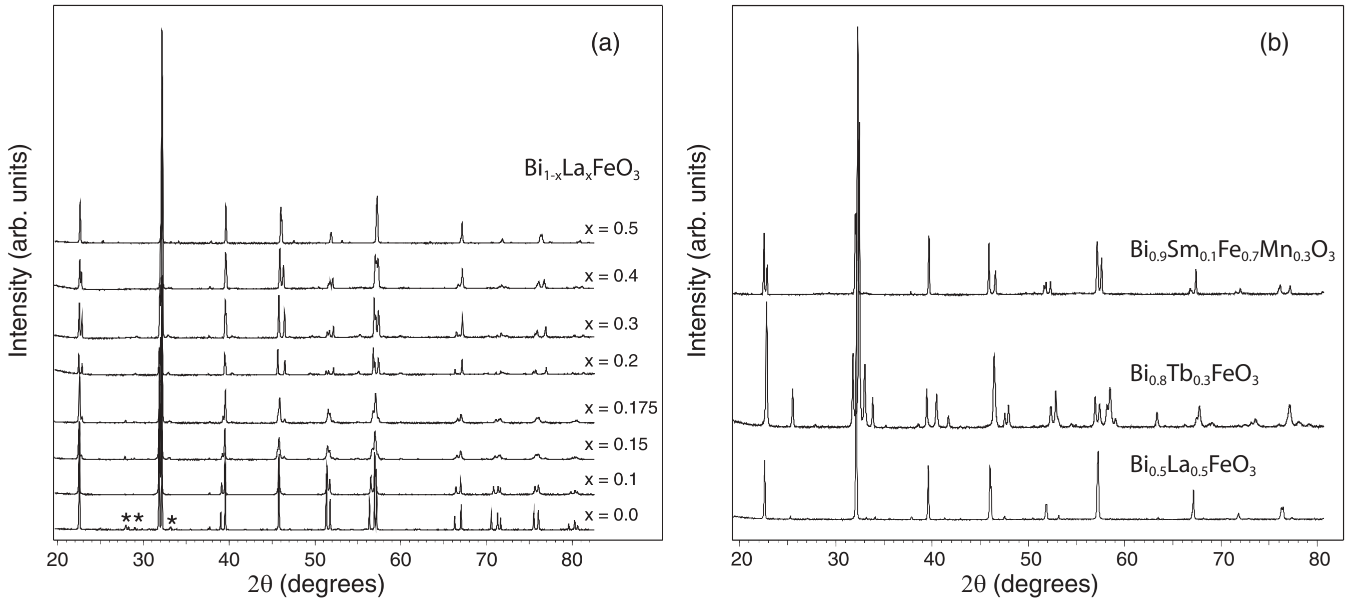

FIG. 1. PXRD data for (a) $Bi_{1-x}La_xFeO_3$ series and (b) $Bi_{0.5}La_{0.5}FeO_3$, $Bi_{0.8}Tb_{0.2}FeO_3$ (both $Pnma$ symmetry), and $Bi_{0.9}Sm_{0.1}Fe_{0.7}Mn_{0.3}O_3$ ($Imma$) from bottom to top. Peaks from the impurity phase $Bi_2Fe_4O_9$ are indicated by $*$ for the $BiFeO_3$ ($x = 0$) sample in (a).

of the recorded spectra, all Raman measurements were recorded at 80 K to minimize additional thermal broadening. The samples were mounted on a cold finger inside a KONTI cryostat type micro from CryoVac and cooled with liquid nitrogen. Additional measurements were recorded at room temperature (not shown) to ensure that no thermally induced phase transition took place at lower temperatures. Plasma lines, as deduced from measurements on a mirror, at 80, and 233 cm^{-1} were manually removed after collecting the spectra. All Raman selection rules presented herein were obtained from the Wyckoff positions in the respective space groups by the SAM tool on the Bilbao Crystallographic Server.[39]

Magnetization versus field and temperature measurements were performed using two Quantum Design systems, a MPMS-XL and a PPMS system. Magnetization (M) vs field (H) measurements were performed at 10 and 300 K between ±50 kOe (MPMS-XL) and/or between ±90 kOe (PPMS). Magnetization versus temperature measurements were performed between 350 and 10 K using an applied field of 500 Oe.

III. X-RAY DIFFRACTION RESULTS

The purity and crystal structure of the $Bi_{1-x}Tb_xFeO_3$ ($0 \leqslant x \leqslant 0.2$) and $Bi_{1-x}La_xFeO_3$ ($0 \leqslant x \leqslant 0.5$) samples prepared for the Raman measurements were assessed on the basis of the long scan PXRD data. For the former series the $x = 0.05$ sample adopted the $R3c$ structure with a trace amount of $Bi_2Fe_4O_9$ detectable. The $x = 0.1$ diffraction pattern was also characteristic of $R3c$, however, very weak signature peaks of the emerging $Pnma$ structure could be discerned. The $x = 0.125$ sample was biphasic containing an approximately 50:50 mixture of $R3c$ and $Pnma$ phases. The $x = 0.15$ sample was predominantly (>90%) $Pnma$, and $x = 0.175$ and 0.2 were phase pure $Pnma$ phases, see Fig. 1(b). These results differ somewhat from those reported in Ref. 15 in that the region of $R3c/Pnma$ phase coexistence is smaller here, and the presence of a minor $Tb_3Fe_5O_{12}$ garnet impurity observed previously for $x \geqslant 0.15$ was avoided. This reflects the advantageous use of a solution based synthesis route. The evolving crystal structures observed for $Bi_{1-x}La_xFeO_3$ samples are apparent from Fig. 1(a). For $x = 0.1$ a $R3c$ phase is obtained with contracted cell parameters compared to $BiFeO_3$. The $x = 0.15$ sample is predominantly $R3c$ but signs of a new structure appear, and these get stronger for the $x = 0.175$ sample where a Rietveld analysis gives 70 wt.% $R3c$. At $x = 0.2$ the structural transformation is complete and the diffraction peaks are well accounted for by the orthorhombic $Pbam$ structure of $PbZrO_3$.[20] This basic structure persists for $x = 0.3$ and 0.4 before the collapse of previously split diffraction lines and the appearance of new peaks, for example, at $2\theta \approx 25^\circ$, indicate the formation of a $Pnma$ phase isostructural with $LaFeO_3$. The general structural dependence on La content is apparently similar to that reported by Rusakov *et al.*[16] and Troyanchuk *et al.*[19] despite the significantly lower final sintering temperature employed here.

The observation of biphasic substitution regions is often seen in similar perovskite series[19,21] and reflects a small energy difference between the two structures that might drive a separation into dopant rich and dopant deficient regions. For this reason, the clearly biphasic samples are excluded from the detailed Raman analysis that follows below.

Globally, then both series of A-site substituted materials display transitions from the ferroelectric $R3c$ structure of $BiFeO_3$ to the orthorhombic and centrosymmetric $Pnma$ structure of $GdFeO_3$. In the process an antiphase tilt along one of the primitive perovskite cell directions is transformed into an in-phase tilt, that is, $a^-a^-a^- \rightarrow a^+b^-b^-$. The final series investigated here, the B-site substituted $Bi_{0.9}Sm_{0.1}Fe_{1-x}Mn_xO_3$, was found to transform to orthorhombic and centrosymmetric

$Imma$ symmetry for $x = 0.3$ via a two-phase region for $x = 0.15$.[21] This transition is consistent with the loss of an antiphase tilt, that is, $a^-a^-a^- \rightarrow a^0b^-b^-$, and as such the $Imma$ structure appears as a natural intermediate between the $R3c$ and $Pnma$ tilts schemes.[21]

IV. RAMAN RESULTS

In this section we present unpolarized Raman spectra on $\mathrm{Bi}_{1-x}\mathrm{La}_x\mathrm{FeO}_3$, $\mathrm{Bi}_{1-x}\mathrm{Tb}_x\mathrm{FeO}_3$, and $\mathrm{Bi}_{0.9}\mathrm{Sm}_{0.1}\mathrm{Fe}_{1-x}\mathrm{Mn}_x\mathrm{O}_3$. Raman spectroscopy offers a powerful tool to distinguish between different space group symmetries. In particular, the number of Raman allowed modes depends strongly on the space group in question and a group theoretical treatment gives the number of Raman active modes in the relevant space groups as follows: $\Gamma_{R3c} = 4A_1 + 9E = 13$, $\Gamma_{Pnma} = 7A_g + 5B_{1g} + 7B_{2g} + 5B_{3g} = 24$, and $\Gamma_{Imma} = 3A_g + 2B_{1g} + 3B_{2g} + 4B_{3g} = 12$ modes where the different phonon symmetries can in principle be separated by their polarization dependencies. Unfortunately the crystallites used in this study were very small and twinned, precluding the identification of the crystal axis and a distinction between the different phonon symmetries could not be made. However, it has previously been shown that $Pnma$ perovskites primarily grow with faces in the pseudocubic ac plane[40] with $\Gamma_{Pnma\text{-}ac} = 7A_g + 7B_{2g} = 14$. The $Imma$ phase exhibits a drastic reduction in the number of observable modes as compared to the $Pnma$ phase, to $3A_g + 2B_{1g}$ in the ab plane, $3Ag + 3B_{2g}$ in the ac plane, and $3A_g + 4B_{1g}$ in the bc plane, while the $R3c$ phase always exhibits at least 13 vibrational modes regardless of crystal face.

A. BiFeO_3-$R3c$

Figure 2 shows 80 K BiFeO_3 spectra from two different micron spots. Comparison between spectra taken at different spots is complicated by the presence of the polarity of the $R3c$ structure that splits the $4A_1 + 9E = 13$ Γ-point phonons into longitudinal (LO) and transverse (TO) branches that vary in both intensity and position as a function of the angle α between the incoming laser light and the [111] pseudocubic crystalline direction [cf. inset Fig. 2(b)]. In total one then finds 22 distinct Raman active phonons, $9E(\mathrm{TO})$ with frequencies independent on α and $9E(\mathrm{LO}) + 4A_1(\mathrm{LO})$ that gradually transforms into $9E(\mathrm{TO}) + 4A(\mathrm{TO})$ as α goes to zero. The allowed number of modes are thus $9E(\mathrm{TO}) + 4A_1(\mathrm{TO}) = 13$ when $\alpha = 0$ and $9E(\mathrm{TO}) + 9E(\mathrm{LO}) + 4A_1(\mathrm{LO}) = 22$ when $\alpha \neq 0$.[33]

With the small crystallites ($\sim$1 μm) used in this study, two spectra typically vary in this regard and each represent different values of α according to the exact orientation of the crystallite face under investigation. Comparing our spectra in Fig. 2 to the extensive study in Ref. 33, we are able to identify the two spectra as arising from α close to 90° (top spectrum) and 54.7° (bottom spectrum)—the latter value is by far the most commonly occurring on our samples and signifies a surface normal to one of the [100], [010], or [001] pseudocubic directions. Similar orientations were observed previously on a polycrystalline BiFeO_3 sample.[41] Looking at the spectra in Fig. 2(a), the first-order phonons are confined to below 600 cm^{-1} with the most characteristic feature being three sharp peaks at approximately 140, 170, and 220 cm^{-1}. One additional pair appears at even lower frequencies, as can be seen in Fig. 2(b). Even though BiFeO_3 has been extensively studied with Raman spectroscopy, the symmetry assignment of the phonon spectrum is still controversial.[23,33] As will be discussed in Sec. V A, we will adopt the assignments from Refs. 33 and 42 (see Fig. 2) as our starting point. Thus, we attribute the three lowest modes to a $E(1)$ doublet at 75 cm^{-1}, a $E(\mathrm{LO2})$ mode at 140 cm^{-1}, and the lowest $A_1(\mathrm{TO1})$ mode, overlapping with the A-site displacement caused by the activation of the Bi lone pair, at 170 cm^{-1}, and they correspond predominantly to Bi motions.[42] Additionally, the atomic motions of the mode

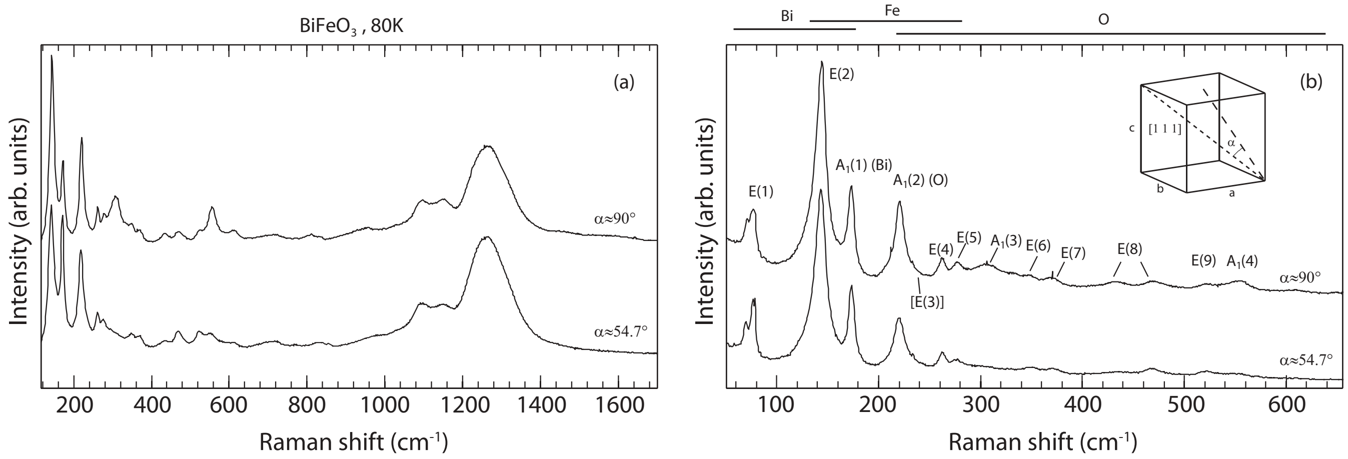

FIG. 2. Raman spectra of BiFeO_3 in the spectral range (a) 130–1700 cm^{-1} and (b) 50–700 cm^{-1} at two different spots. The first-order Γ-point phonons are visible in (a) below 620 cm^{-1}. A strong two-phonon spectrum can be seen at higher wave numbers. A closer look at the first-order phonon is given in (b), together with mode symmetries taken from Ref. 33 and predominantly involved atomic species taken from the first-principle study in Ref. 42. The modes are numbered according to ascending frequency. In addition, as they overlap closely with the polar Bi offset and antiphase oxygen-octahedra distortion respectively,[42] the two lowest A_1 modes are labeled according the main atomic species involved in the vibration. The mode within square brackets was not observed in our spectra, but is included for completeness.[33] The additional modes in the upper spectrum arises as a consequence of the LO-TO splitting of the oblique phonons when the laser light impinges at an angle with the [111] pseudocubic direction.

at 220 cm^{-1} was calculated to originate from an relatively soft oxygen mode with A_1 symmetry that overlap with the $a^-a^-a^-$ oxygen displacement vector. The $A_1(1)$ and $A_1(2)$ modes are thus related to the structural distortions away from the ideal cubic $Pm\bar{3}m$ structure and we will hence refer to these modes as $A_1(1)$(Bi) and $A_1(2)$(O) to indicate the atomic motions present. The phonon assignment in $BiFeO_3$ will be discussed and analyzed in more detail in Secs. V A and V D.

Looking at Fig. 2(a) we also observe strong second-order spectra above 900 cm^{-1}. The origin of the two-phonon scattering is not well understood, but it is clear that it is of a resonant nature[30] and a full description requires the complicated interplay between electron, spin, and lattice degrees of freedom to be taken into account.[27] Additionally, the mode observed at ∼620 cm^{-1} is mysterious in that it does not fit in the Γ-point Raman active vibrations. The assignment of the second-order scattering is discussed in Sec. V D.

B. $LaFeO_3$-*Pnma*

Comprehensive phonon assignments in the *Pnma* structured compound $LaFeO_3$ are already available in the scientific literature.[34,35] In Fig. 3(a) we present $LaFeO_3$ spectra at 80 K that together with the phonon assignments helps us interpret the Raman spectra of the intermediate substituted $Bi_{1-x}La_xFeO_3$ and $Bi_{1-x}Tb_xFeO_3$ samples.

In the *Pnma* structure, 24 Raman active Γ-point phonons are predicted from group theory. Out of these 24 Raman active modes, the 14 $A_{1g} + B_{2g}$ modes are active in the *ac* plane that we expect most of the crystallite surfaces being aligned with. Following Ref. 34 we divide these 14 modes into four groups according to those involving *A*-site vibrations (A), oxygen tilt (T), oxygen bending (B), and oxygen stretch (S), distributed as 6A + 3T + 3B + 2S. The four groups are conveniently separated in energy as indicated in the high-resolution spectrum in Fig. 3(b), where 13 of the 14 modes can be seen; the missing mode is one of the two oxygen stretch modes.

Besides the Γ-point phonons, very strong second-order phonons are observed above 900 cm^{-1}, see Fig. 3(a). Oxygen isotope substitution have conclusively proved that these predominantly involve oxygen vibrations.[34] The appearance of strong second-order scattering is peculiar considering that the strong first-order phonon, ascribed to an antisymmetric stretching motion of the oxygen octahedra, at 625 cm^{-1} has been ruled out as being the source of the second-order scattering.[34] Pronounced second-order scattering without a corresponding Raman active first-order mode have been encountered in a host of perovskites and related oxides and there seems to be several underlying mechanisms responsible for this phenomena.[34,35,43–45] In the case of $LaFeO_3$, a Frölich interaction induced activation of otherwise forbidden LO modes can be used to explain the appearance and position of the second-order scattering.[34,46]

C. $Bi_{1-x}Tb_xFeO_3$

Figure 4 shows the Raman spectra of $Bi_{1-x}Tb_xFeO_3$ in (a) the 130–1700 cm^{-1} and in (b) the 50–375 cm^{-1} frequency range for a Tb content x between $x = 0$ and 0.2. Spectra consistent with the $R3c$ structure are visible up to $x = 0.1$ and the observed features are discussed for $BiFeO_3$ in Sec. IV A. There is however a sudden appearance of a strong mode at 620 cm^{-1} as soon as Tb is introduced at the *A* site. This mode is formally Raman inactive and resonant in nature; a further discussion is found in Sec. V D.

At the other extreme, a clearly different spectrum for $x = 0.2$ can be seen, corresponding to the *Pnma* space group. Comparing the spectra from the two phases, a loss of the low frequency *A*-site vibrations below 200 cm^{-1} and a loss of structure in the oxygen modes between 300 and 600 cm^{-1} is observed, see Fig. 4(a). Looking at the *A*-site vibrations, the two $R3c$ signature peaks between 100 and 200 cm^{-1} disappear and instead a strong band at 320 cm^{-1} appears [Fig. 4(b)]. As will be explained in Sec. V B, this band contains the *Pnma* *A*-site vibrations as well as the oxygen tilt modes.

From a group theoretical perspective, we would expect a similar number of phonons in the two structures, 14 in the *Pnma* *ac* plane compared to 13 in the $R3c$ structure. Thus,

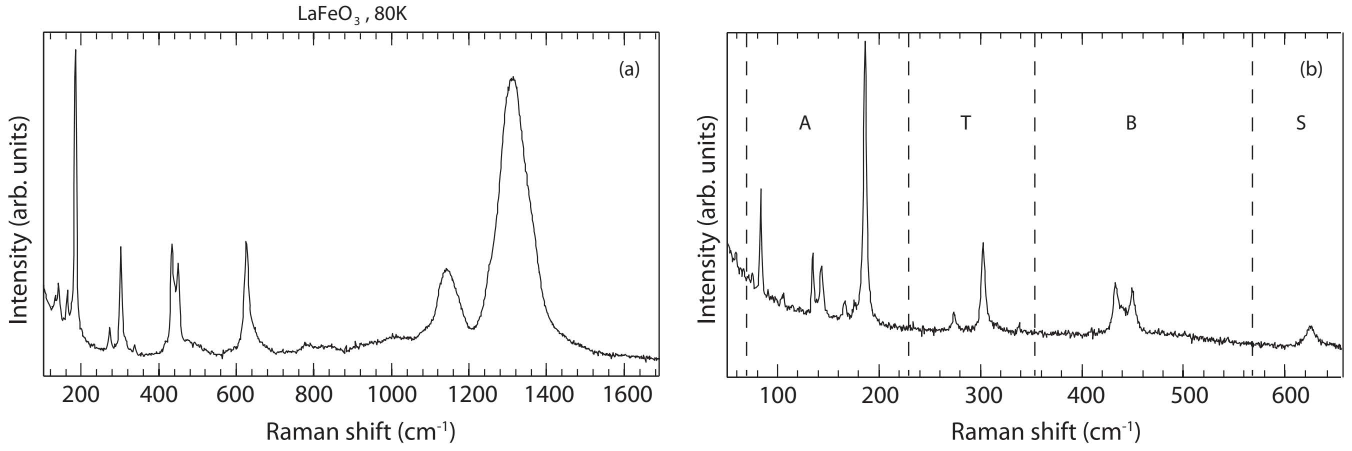

FIG. 3. Raman spectra of $LaFeO_3$ in the spectral range (a) 130–1700 cm^{-1} and (b) 50–700 cm^{-1}. The Raman allowed first-order $A_g + B_{2g}$ phonons in the *ac* plane can be labeled according to the respective atomic motions as either *A*-site modes (A), oxygen tilt (T), oxygen bending (B), or oxygen stretch (S) modes as indicated in (b). Besides the first-order scattering, strong second-order scattering can be observed above 900 cm^{-1} in (a). Notice the broad background beneath the B and T modes arising from IR-active LO vibrations.[34,44,45] These bands becomes Raman active via the Fröhlich interaction and their respective overtones and combinations are the origin of the strong second-order scattering.[34]

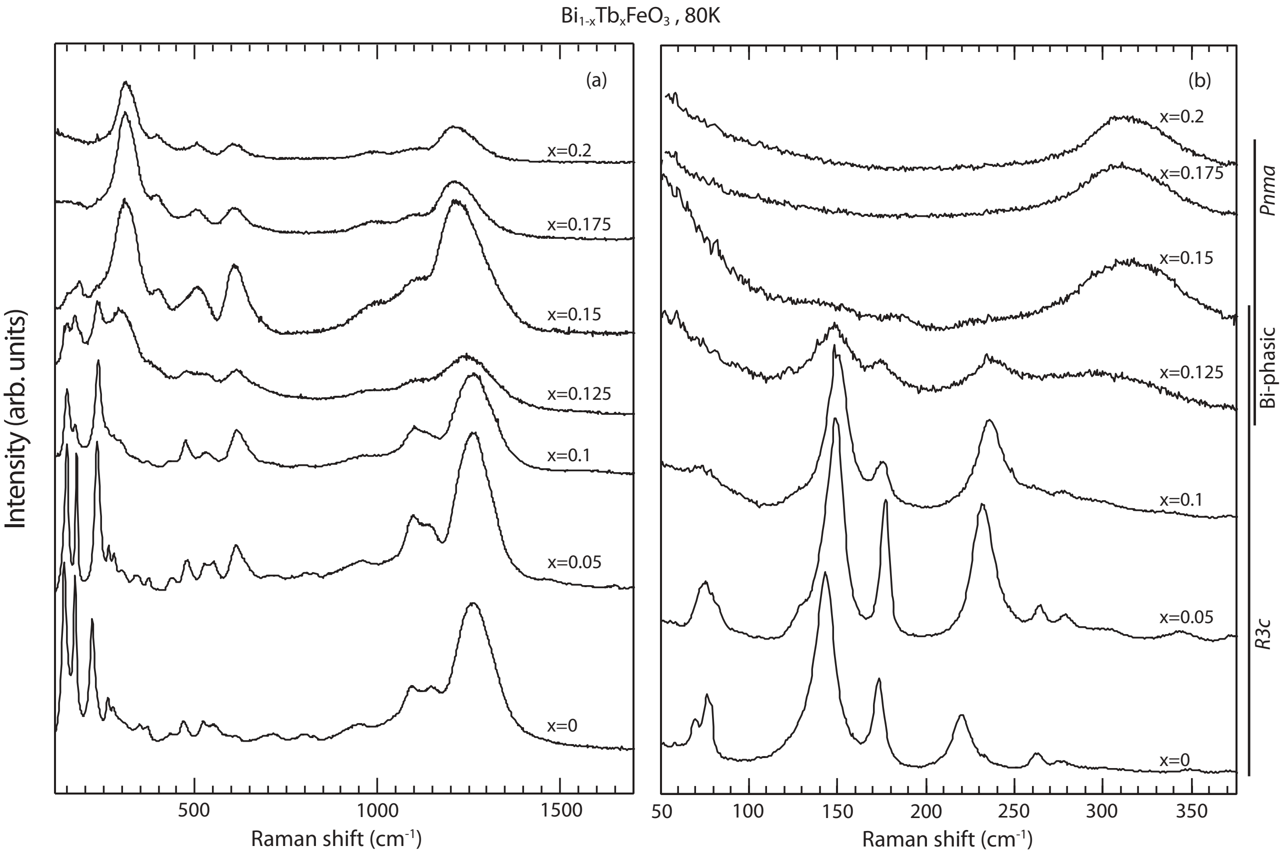

FIG. 4. Raman spectra for $Bi_{1-x}Tb_xFeO_3$ in the spectral range (a) 150–1700 cm^{-1} and (b) 50–375 cm^{-1}. The $R3c$ structure is clearly observed up until $x = 0.1$, while a $Pnma$ structure is seen for $x \geqslant 0.175$. A mixed phase region is found for the intermediate substitution range, indicating phase coexistence on the micron scale. To the right of (b) we indicate the structural phases that each spectrum belongs to. To improve viewing, the individual spectra have been scaled and translated along the y axis.

we attribute the loss of structure to broadening from the Bi-Tb A-site disorder and the concurrent lattice distortion induced by the ionic size mismatch, preventing us from discerning more than the A, T, B, and S regions (in ascending frequency) discussed in Secs. IV B and V B.

In the intermediate Tb range, $0.1 \leqslant x \leqslant 0.175$, the $Pnma$ structure peaks appear gradually alongside the disappearance of $R3c$ signatures as the Tb content is increased. The gradual appearance is especially clear in the 320 cm^{-1} peak that starts to appear at $x = 0.125$, indicating a coexistence between the two phases on a micron scale. For $x = 0.15$, the 320 cm^{-1} peak becomes even more apparent, but a close look at the spectra reveals that a weak trace of the three $R3c$ signature peaks between 140 and 240 cm^{-1} can also be observed here, see Fig. 4 (b). Our observations shows a biphasic composition at $x = 0.125$ and $x = 0.15$, in reasonable agreement with high resolution neutron diffraction data that shows a two-phase region in the Tb range $0.1 \leqslant x \leqslant 0.175$.[15]

D. $Bi_{1-x}La_xFeO_3$

In Fig. 5 we show Raman spectra for $Bi_{1-x}La_xFeO_3$ with x ranging between 0 and 1. From their appearances we divide the spectra into four categories. First, we have $0 \leqslant x \leqslant 0.15$ which exhibit typical $R3c$ spectra, similar what was observed in the Tb series (see Sec. IV C), including the appearance of the strong resonant mode at ~600 cm^{-1} and signs of a phase coexistence at $x = 0.15$. This phase coexistence, most prominently seen in the downshift of the low frequency mode below 100 cm^{-1} and in the appearance of the broad band centered around 280 cm^{-1}, is seen also in the XRD data as discussed in Sec. III.

At slightly higher substitutions we have the second category for x between 0.175 and 0.2. In this substitution range, the two sharp $R3c$ A-site modes below 200 cm^{-1} gives way to two overlapping phonons positioned at approximately 160 and 180 cm^{-1}, respectively. The A-site mode at 75 cm^{-1} downshifts 15 cm^{-1} at the same time as it increases in intensity and undergoes a drastic change in line shape, see Fig. 5(b). Above these frequencies an increase in the observed spectral structure can be observed in the whole frequency range. This is most apparent in a strong peak at 290 cm^{-1} together with a pronounced two-peak structure in the 1200 cm^{-1} band, see Fig. 5(a). This two-peak structure is mirrored in the oxygen breathing region slightly above 600 cm^{-1}, hinting at the origin of the second-order scattering, see Sec. V D for additional comments. We note an apparent discrepancy between the Raman and x-ray diffraction results for the $x = 0.175$ sample. The Raman spectra displays clear signatures of a $PbZrO_3$-type structure while the phase fractions estimated from the x-ray

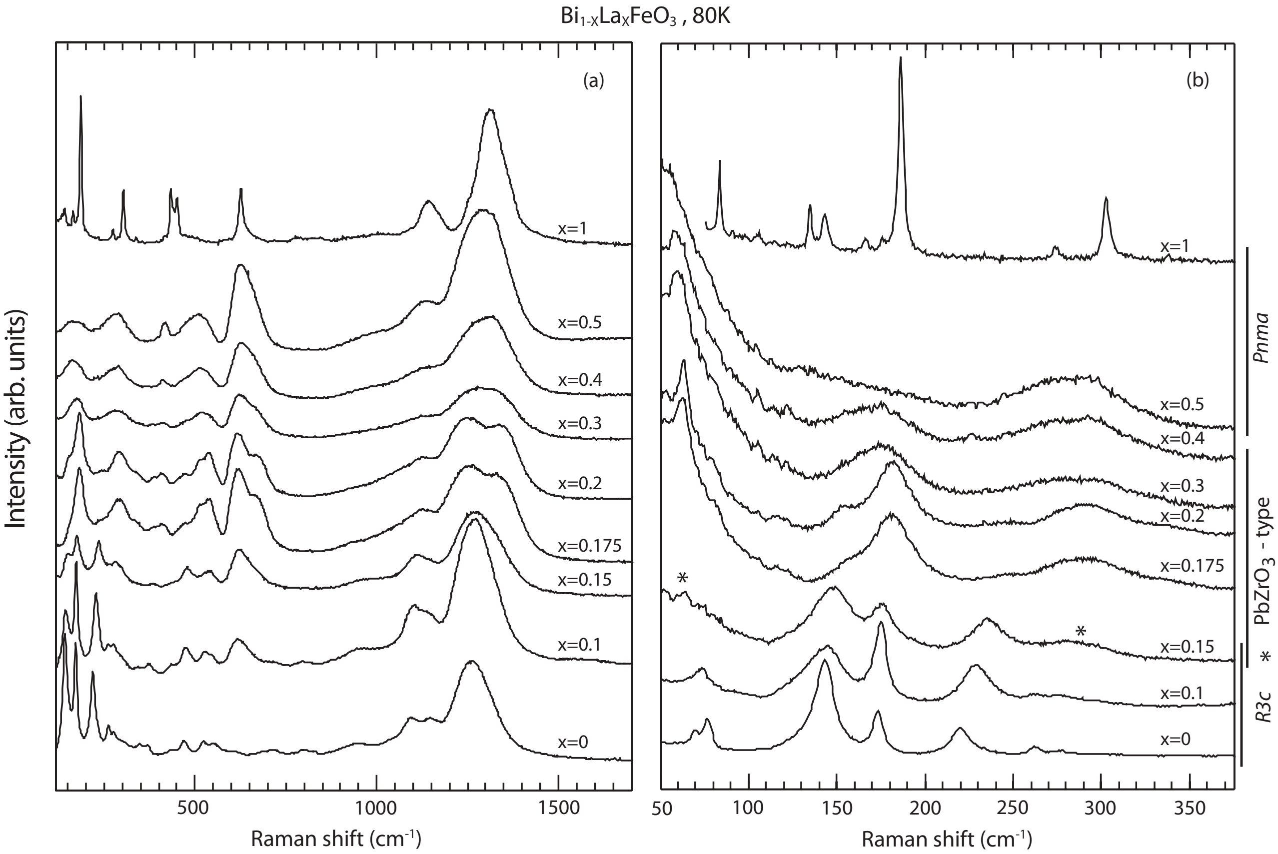

FIG. 5. Raman spectra for $Bi_{1-x}La_xFeO_3$ in the spectral range (a) 150–1700 cm^{-1} and (b) 50–375 cm^{-1}. The spectra indicates a $R3c$ structure below $x \leqslant 0.15$. From the high resolution spectra in (b), a centrosymmetric $Pnma$ structure can be deduced for $x \geqslant 0.5$, while the low frequency mode at 60 cm^{-1} indicates an antiferroelectric structure between $x = 0.175$ and $x = 0.4$, see Sec. V. To the right of (b) we indicate the structural phases that each spectrum belongs to. Stars are used in the biphasic $x = 0.15$ sample to highlight the Raman active modes characteristic of the $PbZrO_3$-type phase. To improve viewing, the individual spectra have been scaled and translated along the y axis.

diffraction indicate the sample is predominantly (∼70 wt.%) $R3c$. We attribute this to domain sampling in the Raman measurements. Only a small portion of the sample surface, as viewed under the microscope, exhibited smooth crystal surfaces of a sufficient size to focus onto. Even though several spectra were taken at individual crystallites for every substitution level, there is a bias towards sampling of the larger crystallites. Consequently, it is possible that the dominant $R3c$ phase forms smaller crystallites than the relatively minor $PbZrO_3$-type phase in the $Ba_{0.825}La_{0.175}FeO_3$ compound under the synthesis condition used.

Increasing the substitution level further, a third spectral category is reached for $0.3 \leqslant x \leqslant 0.4$. In many ways, the $x = 0.3$ spectrum has features akin to a broadened version of the category two spectra, while still keeping the sharp low frequency mode at 60 cm^{-1}. Approaching $x = 0.5$, the 60 cm^{-1} mode disappears and the spectrum broadens further, keeping only four broad bands at 170, 280, 500, and 625 cm^{-1} and one sharper peak at 420 cm^{-1}. The strong low frequency tail in Fig. 5(b) has its origin in elastically scattered laser light and the increase of this tail with increased substitution level can, at least partly, be attributed to a decreased particle size with increased A-site substitution as observed under the microscope. As stated above, the spectral features in $LaFeO_3$ can be clearly divided into four well defined clusters, see Fig. 3 and the accompanying discussion. A clear correspondence between the features at 170, 280, 420, and 625 cm^{-1} in the $x = 0.5$ spectrum visible in Fig. 5(a) and the four clusters in the $LaFeO_3$ spectrum can be made. Judging from previously published spectra of the $x = 0.6$ and $x = 0.8$ compounds,[36] we attribute the fifth band, located at 500 cm^{-1}, as of the same origin as the broad LO background that overlaps with the 450 cm^{-1} mode group in $LaFeO_3$, see the discussion in Sec. V B.

E. $Bi_{0.9}Sm_{0.1}Fe_{1-x}Mn_xO_3$

Raman spectra of $Bi_{0.9}Sm_{0.1}Fe_{1-x}Mn_xO_3$ for $0 < x \leqslant 0.30$ together with $BiFeO_3$ is shown in Fig. 6. Incorporation of 10% Sm on the A-site produces a $R3c$-type Raman spectrum very similar to what is observed in the case of small levels of La and Tb substitution. As soon as Mn is introduced at the B site, the spectral features become fewer, broaden, and decrease in intensity. The decrease in the observed number of peaks is consistent with the $R3c$ to $Imma$ transition,[21] which should be accompanied by a decrease in the number of allowed Raman active modes from 13 in $R3c$ to between five and seven in $Imma$, depending on the surface orientation.

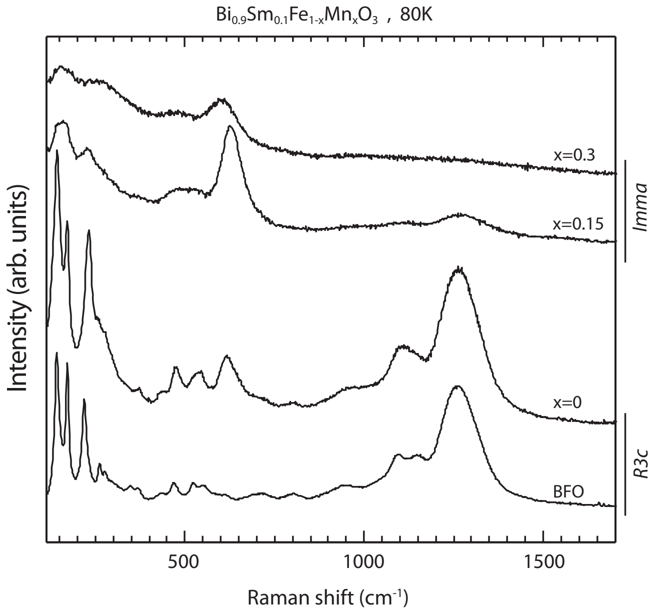

FIG. 6. Raman spectra for $Bi_{0.9}Sm_{0.1}Fe_{1-x}Mn_xO_3$ and $BiFeO_3$ in the spectral range 150–1700 cm^{-1}. The transition from $R3c$ to $Imma$ symmetry is clearly visible in the decrease in spectral features above $x = 0.15$. To the right we indicate the structural phases that each spectrum belongs to, although a phase coexistence in the $x = 0.15$ sample, in accord with results from neutron diffraction,[21] can be deduced from the observable, but weak, second-order scattering. To improve viewing, the individual spectra have been scaled and translated along the y axis.

However, the more recently reported $Pnam$ and incommensurate structures[22] for the same series with larger unit cells and lower symmetries are not compatible with the decrease in observed spectral features. We interpret the discrepancy between the diffraction studies as a manifestation of a large structural sensitivity in these materials to the exact conditions during sample synthesis.

It is also interesting to note the huge decrease in the resonant second-order scattering when Mn is introduced, see Fig. 6. Neutron diffraction data on the $x = 0.15$ sample have previously shown a mixed $R3c$-$Imma$ phase.[21] Although weak, the second-order scattering in the $x = 0.15$ sample can thus be assigned to the $R3c$ phase, while the second-order scattering is absent in the $Imma$ phase. Consistent with this, the much more pure $Imma$ phase in the $x = 0.3$ sample shows almost no signs of any second-order scattering.

V. RAMAN DISCUSSION

A. Structural effects and phonon assignments in the *R3c* phases

A collection of high resolution spectra in the range 50–300 cm^{-1} of the $R3c$ structure samples $BiFeO_3$, La10, La15, Tb5, Tb10, and Sm10, focusing on the low frequency modes, whose positions in $BiFeO_3$ are marked by dashed lines, can be found in Fig. 7. Several differing assignments of the phonon spectrum in this region can be found in the literature. In Ref. 42, first-principle calculations[42] were used to assign these modes to the $E(1)$ doublet at 80 cm^{-1}, the $E(2)$ doublet at 140 cm^{-1}, the A_1(LO1) at 175 cm^{-1}, and the A_1(LO2) at 220 cm^{-1}. The same assignment was obtained in the experimental study by Hlinka *et al.*[33] However, Beekman *et al.*[23] found a differing assignment where all four modes were attributed to E(TO) modes, and the lowest A_1 mode was instead assigned to the weak 260 cm^{-1} vibration seen in Fig. 7.

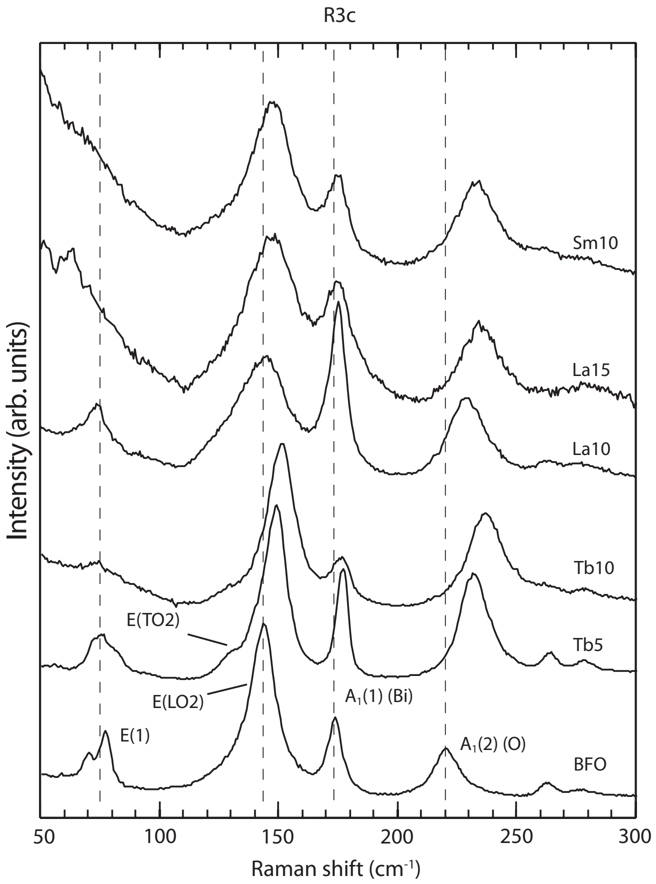

FIG. 7. Comparison of the low frequency spectra in the $R3c$ structures of $BiFeO_3$, $Bi_{1-x}Tb_xFeO_3$, $Bi_{1-x}La_xFeO_3$, and $Bi_{0.9}Sm_{0.1}FeO_3$ collected at 80 K. Dashed lines shows phonon positions in $BiFeO_3$ and are used to facilitate comparison between samples. The LO-TO splitting is visible as a two peak structure in the $E(1)$ mode and as the shoulder of the $A_1(1)$ mode for the $E(2)$ mode. To improve viewing, the individual spectra have been scaled and translated along the y axis.

A general feature of perovskites in the $Pnma$ and $R\bar{3}c$ structures is a strong frequency dependence on the octahedral tilt angle, resulting in shifts of more than 20 cm^{-1} per deg, of the pseudosoft octahedral A_1 tilt mode around the [111] direction,[47] and indeed a strong shift/angle correlation for the A_1 [111] tilt mode was found also in the closely related $R3c$ structure of $BiFeO_3$ by first-principle calculations.[48] The $a^-a^-a^-$ oxygen tilt angle along [111] changes from $\sim 12.1^\circ$ in BFO[49] to 13.1° in Tb10,[15] and a corresponding ~ 20 cm^{-1} shift of the A_1 [111] tilt mode is thus expected between these samples.

By collecting all $R3c$ spectra from the substitution series, we obtain in this way new input for the phonon assignments in $BiFeO_3$ related materials. Indeed, the most noticeable effect upon substitution on the A site is the drastic shift in frequency of the 220 cm^{-1} mode, which we consequently assign as the

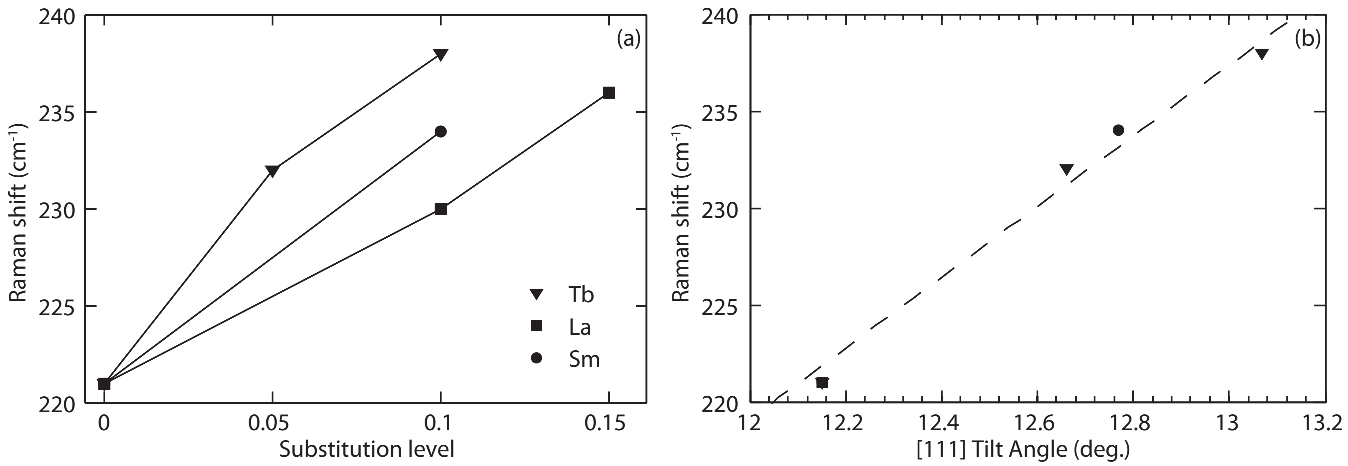

FIG. 8. (a) Position of the $A_1(2)(O)$ mode as a function of A-site substitution for the BFO, Tb5, Tb10, La10, La15, and Sm10 samples. The shift due to Tb substitution is significantly larger than that from La substitution as is expected from the increased octahedral distortion in $Bi_{1-x}Tb_xFeO_3$. (b) Shows the same Raman shifts, now as a function of the octahedral tilt angle. The near linear dependence, with a slope of 18 cm^{-1}/deg, indicates a close connection between the frequency of the $A_1(2)(O)$ mode and the octahedral distortion in the $R3c$ structure. The tilt angles were extracted from room temperature neutron diffraction studies,[15,21] however, no reliable data on the La containing materials could be found.

A_1 [111] tilt mode, while all other peak frequencies exhibit relatively small shifts. This mode is clearly observed in all $R3c$ samples, and it shifts from 220 cm^{-1} in BFO to 238 cm^{-1} in Tb10, see Fig. 8(a). Furthermore, the expected correlation between the [111] tilt angle and $A_1(2)(O)$ frequency is highlighted in Fig. 8(b), where also a linear fit with slope 18 cm^{-1}/tilt deg is shown.

As can be expected from a simple ionic size argument, where the octahedral distortion, including the octahedral tilt, increases when the size difference between A-site cations increases, the largest shift is observed in $Bi_{1-x}Tb_xFeO_3$ followed by $Bi_{0.9}Sm_{0.1}FeO_3$ and $Bi_{1-x}La_xFeO_3$ displays the smallest shift, see Fig. 8(a). While explaining the relative changes in Raman shift of the $A_1(2)(O)$ mode, this simple argument does not explain the shift induced by the very similarly sized La^{3+} cation compared to the Bi^{3+} cation. Here we must remember that the activation of the Bi lone pair and the corresponding [111] displacement of the Bi atoms depends on a Bi s-O p/s hybridization[9] that in itself affects the unit cell parameters. Dilution of the lone pair with A-site substitution will thus alter the octahedral arrangement even in the absence of direct lattice deformations through a contraction of the unit cell, resulting in the observed shift of the $A_1(2)(O)$ mode even when lattice distortions from ionic size mismatch at the A site are expected to be small.

We believe that our independent assignment of A_1 symmetry to the 220 cm^{-1} mode strengthens the assignments by Hlinka *et al.*,[33] while at the same time, at least partially, falsifying the assignments by Beekman *et al.*[23] It should be noted that the assignments in Ref. 23 rests on fitting the angular dependence on the phonon intensities to the $R3c$ Raman tensors. However, the Raman tensors used in Ref. 23 contains a large antisymmetric component, while vibrational Raman tensors should be completely symmetric,[50] putting further doubts about the validity of the assignment provided there. Indeed, phonon assignments in $BiFeO_3$ using nearly the same technique but symmetric Raman tensors gives an assignment in line with the one adopted in this article.[41]

Turning our attention towards the $E(1)$ mode at 75 cm^{-1}, we clearly see the LO-TO splitting in $BiFeO_3$ in Fig. 7. With Tb substitution, the splitting becomes less pronounced at 5% substitution and at 10% Tb content the intensity becomes too low for an eventual splitting to be observed, but it is clear that the $E(1)$ mode does not shift significantly in frequency as a consequence of Tb substitution. This still holds true for 10% La substitution, whereas the mode suddenly disappears at 15% La. At this substitution level the $E(1)$ at 75 cm^{-1} is instead replaced by a mode belonging to the antiferroelectric $PbZrO_3$-type phase at 60 cm^{-1} due to the phase coexistence discussed in Sec. IV D. Overall, the intensity of the 75 cm^{-1} $E(1)$ mode, whose atomic motions can be described as an antiphase vibration between the A site and FeO_6 sublattices,[28] decreases with substitution level. A similar intensity decrease is found for the weak B-site mode at 260 cm^{-1}. The concurrent intensity decrease of the B-site involving modes could be due to a decoherence of the long range noncentrosymmetric displacement of the B-site ion as the Bi lone pair is diluted—the B-site vibrations are Raman silent in a centrosymmetric octahedral coordination. The partial destruction of the spin cycloid indicated by the magnetization data of $Bi_{0.9}Sm_{0.1}FeO_3$ (Sec. VI) could be related to this effect and points towards a connection between the spin cycloid and the B-site atomic position through the nonuniform ferroelectric polarization induced by A-site substitution.

B. Band assignments in the *Pnma* phases

In this section we analyze and make mode assignments of the Raman spectra from the different *Pnma* phases, based on the $LaFeO_3$ spectrum that was discussed in detail in Sec. IV B.

High frequency Raman spectra of the *Pnma* phases $LaFeO_3$, $Bi_{0.8}Tb_{0.2}FeO_3$, and $Bi_{0.5}La_{0.5}FeO_3$ are collected in Fig. 9. The first-order $LaFeO_3$ spectrum is divided in the

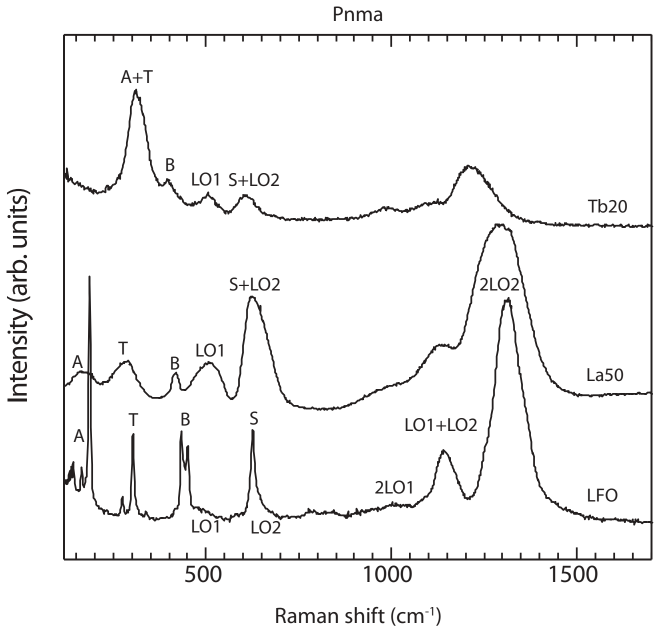

FIG. 9. Band assignments in the *Pnma* phases of $\mathrm{LaFeO_3}$, $\mathrm{Bi_{0.8}Tb_{0.2}FeO_3}$, and $\mathrm{Bi_{0.5}La_{0.5}FeO_3}$ collected at 80 K. The labeling of A, T, B, and S is explained in Fig. 3. LO denotes the Raman-inactive longitudinal phonons whose overtones and combination bands are the source of the second-order scattering,[34,46] see text for details. To improve viewing, the individual spectra have been scaled and translated along the y axis.

four mode groups A (A-site), T (oxygen tilt), B (oxygen bending), and S (oxygen stretch) as discussed in Sec. IV B. In addition,the Frölich activated Raman forbidden longitudinal modes LO1 and LO2, and the corresponding second-order modes 2LO1, LO1 + LO2, and 2LO2 can be seen in Fig. 9.

The mode assignment in the substituted compounds is summarized in Fig. 9 and uses the second-order scattering above 900 $\mathrm{cm^{-1}}$ to first assign the formally Raman inactive LO modes, whereafter the A, T, B, and S bands can be assigned.

The simultaneous downshift of the S + LO2 and 2LO2 mode in $\mathrm{Bi_{0.8}Tb_{0.2}FeO_3}$ implies that the S + LO2 band is mainly of LO2 character. Furthermore, the similar shapes of the S + LO2 bands and the 2LO2 bands in both $\mathrm{Bi_{0.8}Tb_{0.2}FeO_3}$ and $\mathrm{Bi_{0.5}La_{0.5}FeO_3}$ provides additional support for this view.

The position of the 2LO1 and LO1 + LO2 bands implies that the strong ~500 $\mathrm{cm^{-1}}$ band in $\mathrm{Bi_{0.8}Tb_{0.2}FeO_3}$ and $\mathrm{Bi_{0.5}La_{0.5}FeO_3}$ is the LO1 mode. For $\mathrm{Bi_{0.5}La_{0.5}FeO_3}$, the remaining three bands below 500 $\mathrm{cm^{-1}}$ coincides in frequency with the A, T, and B bands in $\mathrm{LaFeO_3}$ and are thus assigned accordingly. The situation for $\mathrm{Bi_{0.8}Tb_{0.2}FeO_3}$ is different as there are only two observed bands, at 310 and 400 $\mathrm{cm^{-1}}$, respectively, that could be assigned to the A, T and B mode groups. As it lies very close in position to the B mode group observed in both $\mathrm{LaFeO_3}$ and $\mathrm{Bi_{0.5}La_{0.5}FeO_3}$, the 400 $\mathrm{cm^{-1}}$ band is assigned to the B modes. The remaining strong band at 310 $\mathrm{cm^{-1}}$ must therefore be assigned to overlapping A and T bands, see Fig. 9.

As the Bi lone pair should be long-range inactive in the centrosymmetric *Pnma* structure it is not surprising that $\mathrm{LaFeO_3}$ and the mixed La-Bi sample, with very similar ionic radii, exhibit correspondingly similar spectral positions in their respective Raman spectrum. We consequently interpret the upshift of the A band and the downshift of the 2LO2 band in $\mathrm{Bi_{0.8}Tb_{0.2}FeO_3}$ as a sign of the lattice distortions induced by the differences in the $\mathrm{Bi^{3+}}$ and $\mathrm{Tb^{3+}}$ ionic radii.

C. The La20 structure

The structural phase transition away from the $R3c$ symmetry, when increasing the La content, has recently been a matter of discussion in the literature. From electron diffraction, Rusakov *et al.*[16] observed a $\mathrm{PbZrO_3}$-type *Pnam* structure at 18% La content while a incommensurately modulated structure based on *Imma* was claimed between 19% and 30%. On the other hand, Troyanchuk *et al.*[18] observed a similar antipolar, probably incommensurate, structure all the way between 20% and 45% La. A $\mathrm{PbZrO_3}$-type structure was also observed by Karimi *et al.*[17] when 20% Nd and 15% Sm was introduced at the A site.

Here we would like to clarify the notion of the $\mathrm{PbZrO_3}$ type structure, which can be used to denote both the *Pbam* and *Pnam* structures. Both structures shares antipolar cation displacements along the pseudocubic $[110/\bar{1}\bar{1}0]$ directions. However, the *Pnam* structure has a combined $a^-a^-c^+/a^-a^-c^-$ tilt system of the oxygen octahedra and a unit cell quadrupled along c of dimension $\sqrt{2}a \times 2\sqrt{2}a \times 4a$. *Pbam* has a simpler $a^-a^-c^0$ tilt system and a correspondingly smaller unit cell doubled along c, of dimension $\sqrt{2}a \times 2\sqrt{2}a \times 2a$. $\mathrm{PbZrO_3}$ crystallizes in the *Pbam* structure,[51] but because of the similar cation displacements and octahedral tilts, the *Pnam* structure is also referred to as being of "$\mathrm{PbZrO_3}$type."

Motivated by the clues from diffraction data, we decided to directly compare the Raman spectrum of $\mathrm{Bi_{0.8}La_{0.2}FeO_3}$ with that from $\mathrm{PbZrO_3}$.[52] As can be seen in Fig. 10, there are striking similarities between the two spectra. In the region above 100 $\mathrm{cm^{-1}}$ it is possible to map the spectral features in

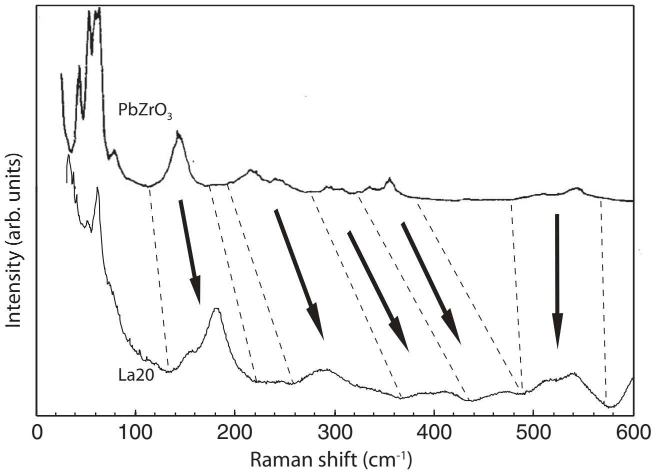

FIG. 10. Comparison between $\mathrm{PbZrO_3}$ at 273 K (top) and $\mathrm{Bi_{0.8}La_{0.2}FeO_3}$ at 80 K (bottom). Notice the similarity in spectral features shared between the two compounds as indicated by the arrows and dashed lines, including the presence of low-frequency antiferroelectric modes below 100 $\mathrm{cm^{-1}}$. The Raman spectrum of $\mathrm{PbZrO_3}$ was reproduced from the spectrum found by Pasto and Condrate.[52]

$PbZrO_3$ to those in $Bi_{0.8}La_{0.2}FeO_3$ as is illustrated with the arrows in Fig. 10. The large relative downshift in $PbZrO_3$ can be explained by different magnitudes of the lattice distortions as well as the close to twice as heavy Zr atom compared to Fe. Indeed, shifts of this magnitude is observed in many isostructural perovskites along with near constant frequencies of the oxygen stretch modes between 500 and 600 cm^{-1}.[53,54] Also, the A-site disorder in $Bi_{0.8}La_{0.2}FeO_3$ accounts for the more diffuse peaks compared to those in $PbZrO_3$.

Below 100 cm^{-1} $PbZrO_3$ shows a large number of peaks speculated to originate from antiferroelectric displacements.[52] A single low frequency peak positioned at 80 cm^{-1} of antiferroelectric origin was also observed in the antiferroelectric perovskite $Sr_{0.70}Ca_{0.30}TiO_3$.[55] Consistent with these related compounds, we assign the 60 cm^{-1} mode in $Bi_{0.8}La_{0.2}FeO_3$ to an antiferroelectric displacement of the A site.

Taken together, the Raman spectra indicates a large similarity between the $Pbam$ and $Bi_{0.8}La_{0.2}FeO_3$ structures. The doubling of the unit cell as we go from $Pbam$ to $Pnam$ should be accompanied by an increase in the number of normal modes. The lack of additional Raman modes in the $Bi_{0.8}La_{0.2}FeO_3$ spectrum as compared to the $PbZrO_3$ spectrum can in this context be interpreted as an indication that any eventual c^+/c^- octahedral tilt is too small or incoherent to generate strong additional Raman allowed modes. However, as the Raman spectrum is also sensitive to the local environment, even incoherent tilts should give rise to additional Raman modes. Thus, we claim that $Bi_{0.8}La_{0.2}FeO_3$ has a structure of the $PbZrO_3$ type, with any c^+/c^- oxygen tilts in $Pnam$ being too small to detect with the methods employed here.

On increasing the La content, it becomes difficult to tell from the first-order spectra in Fig. 5(a) if the broadened Raman spectra in the range between 30% and 50% La belongs to the centrosymmetric $Pnma$ or the antipolar $PbZrO_3$-like structure. From the perseverance of the antiferroelectric mode at 60 cm^{-1} [see Fig. 5(b)] it is clear however that an antipolar structure is retained at least until 40% La, while the broadening of the spectra implies a disordered crystal structure with Raman signature very similar to the $Pnma$ phase at 50% La content. The lack of spectral differences at high frequencies between the 40% and 50% La spectra makes it possible to extend the band assignment for the $Pnma$ structure to the $PbZrO_3$-type structure discussed here. It is however not clear whether any of the LO1 and LO2 bands are still Raman forbidden LO modes activated by the Frölich interaction or if they are Raman allowed LO phonons in the antipolar $PbZrO_3$-like structure.

Comparing to $Bi_{1-x}Tb_xFeO_3$, the lack of the 60 cm^{-1} feature in the Tb substitutes samples is a a sign of the complete transition to the centrosymmetric $Pnma$ structure as soon as the $R3c$ structure becomes destabilized by the large ionic size difference.

D. Second-order scattering

As can be seen in Figs. 4(a), 5(a), and 6, strong second-order scattering was observed above 900 cm^{-1} in all samples except the Mn-containing $Bi_{0.9}Sm_{0.1}Fe_{1-x}Mn_xO_3$. From this straightforward observation it is clear that the B-site cation has a major impact on the appearance of the second-order scattering. Likewise, suitable B-site substitution in related perovskites can greatly enhance both second- and higher order scattering.[34,35,43] Furthermore, the second-order scattering has been shown, in both $BiFeO_3$ and $LaFeO_3$, to be of a local and resonant character, indicating a charge-transfer driven resonant activation of local oxygen breathing modes and their second harmonics and combinations.[30,34] Nevertheless, a detailed mode assignment is lacking[56] for $BiFeO_3$ and in particular the vibrational mode at ∼620 cm^{-1} requires an explanation as it does not fit in the expected Raman allowed Γ-point phonons.[33]

Figure 11 highlights the second-order scattering as well as the corresponding first-order spectra from the noncentrosymmetric $BiFeO_3$, $Bi_{0.95}Tb_{0.05}FeO_3$ (both with $R3c$ structure), $Bi_{0.8}La_{0.2}FeO_3$ of $PbZrO_3$-type structure, and $LaFeO_3$ of the centrosymmetric $Pnma$ structure. The observed first-order modes, M1, M2, and M3 in ascending frequency, and the second-order modes, denoted with suitable combinations of the first-order modes, are shown. For $LaFeO_3$ the already reported mode assignment is used as as a reference.[34]

In $LaFeO_3$, the vibrations responsible for the second-order scattering are the IR active longitudinal optical LO1 and LO2 breathing modes[34,35] that are formally Raman inactive but become Raman active as a consequence of the Frölich interaction.[46] The LO1 and LO2 modes can be seen as the broad bands, partially overlapping with Raman active Γ-point phonons, centered at ∼470 and 620 cm^{-1}, respectively, in Fig. 11. In the polar $R3c$ structure on the other hand, all IR active vibrations are also Raman active due to the loss of inversion center but in addition there also exists the completely silent A_2 modes. Thus, even though a similar explanation of the second-order scattering might be valid for both the centrosymmetric and noncentrosymmetric cases, the LO modes giving rise to the strong second-order scattering are not necessarily Raman forbidden in the noncentrosymmetric $R3c$ and $PbZrO_3$-type structures.

The second-order scattering in $BiFeO_3$ shows five clearly visible modes above 900 cm^{-1} and a sixth one can be deduced from the line shape at 1100 cm^{-1}. We attribute the six second-order modes to the combination modes and overtones produced by three first-order modes positioned approximately at 470, 550, and 620 cm^{-1}, respectively, labeled M1, M2, and M3 in Fig. 11, where the dashed lines shows the positions of the first- and second-order scattering in $BiFeO_3$. Notice also the little to no change in the second-order scattering when going from $\alpha \approx 54.7^\circ$ (broken line) to $\alpha \approx 90^\circ$ (solid line), even though M2 increases drastically in intensity when $\alpha \approx 90^\circ$.

Substituting 5% Tb on the A site produces no qualitative changes in the second-order spectrum as can be seen in the Tb5 spectrum in Fig. 11. There are however two noticeable differences in the first-order modes. First, we observe a ∼10 cm^{-1} upshift of the M1 mode that occurs together with an upshift of the corresponding overtones and combination bands 2M1, M1 + M2, and M1 + M3, while the M2 and M3 modes are constant in frequency. This validates our attribution of the second-order 2M1 mode to the correct first-order M1 mode. Second, a resonant enhancement of the M3 mode takes place. This resonant enhancement can be seen in all substituted spectra and has also been observed in B-site substituted $LaFeO_3$.[34] Comparing with $LaFeO_3$, the LO1 and LO2 modes roughly coincide with the M1 and M3 modes in frequency, while M2 seems to be absent.

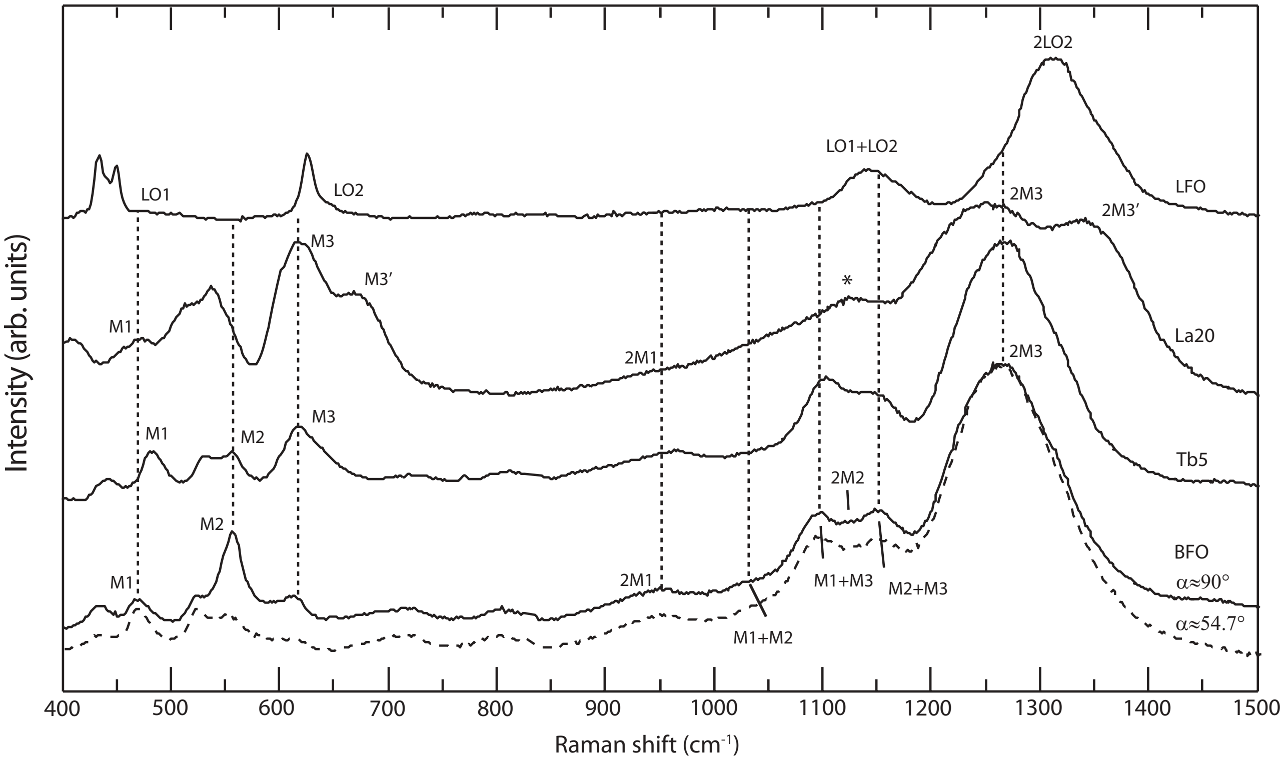

FIG. 11. Raman spectra in the region of second-order scattering in $BiFeO_3$, $Bi_{0.95}Tb_{0.05}FeO_3$, $Bi_{0.8}La_{0.2}FeO_3$, and $LaFeO_3$. The second-order scattering is attributed to overtones and combination modes of the first-order modes M1, M2, and M3. In total there are six expected peaks in the second-order scattering: 2M1, 2M2, 2M3, M1 + M2, M1 + M3, and M2 + M3. The dashed lines indicates the position of the first and five of the expected second-order modes in $BiFeO_3$, while the sixth 2M2 peak is hinted in the line shape between the M1 + M3 and M2 + M3 modes. The $Bi_{0.95}Tb_{0.05}FeO_3$ spectrum is very similar to the $BiFeO_3$ spectrum except from a shift in the M1 related modes and resonant enhancement of the M3 mode. $Bi_{0.8}La_{0.2}FeO_3$ shows a distinct double peak structure in the first-order M3 mode and the overtone 2M3, denoted by M3′. The M1 and 2M1 peaks are also visible, while the decrease in spectral features indicates the absence of the M2 mode. The M1 + M3 and M1 + M3′ peaks forms a featureless band with just one visible peak, marked with a star. The resonant enhancement of the M3 mode in $Bi_{0.95}Tb_{0.05}FeO_3$ and $Bi_{0.8}La_{0.2}FeO_3$ is very similar to what is observed in *B*-site substituted $LaFeO_3$,[34] and leads us to assign the M3 mode to a formally Raman-silent A_2 LO mode. A common mechanism behind the different second-order peak suggests a LO assignment of all of the M1, M2, and M3 modes.

A clear two-peak structure is apparent when inspecting the second-order spectrum of the $PbZrO_3$-type structured $Bi_{0.8}La_{0.2}FeO_3$. The two-peak structure is mirrored exactly in the first-order M3 mode, leaving no doubt that the resonantly enhanced M3 mode is responsible for the strong second-order scattering between 1200 and 1400 cm^{-1}. The M1 mode and its overtone 2M1 are again at nearly the same positions as in $BiFeO_3$, while their combination mode M3 + M1 and M3′ + M1 forms a featureless band as indicated by a star in Fig. 11. From the decrease in structure in the second-order spectrum, we deduce that the M2 mode is not present here, similar to what is observed for the *Pnma* structure.

The M2 mode at 550 cm^{-1} in $BiFeO_3$ has previously been assigned to either the $A_1(4)$ TO mode[33] or to the $E(9)$ LO mode.[42,57] The M3 mode at 618 cm^{-1} was found to not fit in the Γ-point allowed modes for $BiFeO_3$.[33] From previous mode assignments for $BiFeO_3$ it is therefore probable that the M3 mode is a Fröhlich activated mode, while the symmetry of the M2 mode is ambiguous. Furthermore, no conclusions about the M2 mode can be drawn from the second-order scattering in the centrosymmetric *Pnma* structure as it is not visible there, see Fig. 11. However, the M1 mode has previously been assigned to the $E(8)$ LO mode in $BiFeO_3$.[33] This is further supported by the LO assignment of the broad band at similar energy in the *Pnma* structured $LaFeO_3$. Analogously, the similar energy of the LO2 mode in $LaFeO_3$ and the M3 modes suggests a Fröhlich interaction activated A_2 LO assignment of the M3 mode. This last assertion is supported by first-principles calculations that predicts the highest A_2 mode to lie between 620 and 700 cm^{-1}, depending on the functional used. Hence, the common Fröhlich mechanism responsible for the second-order scattering over the whole substitution range imply the $E(9)$ LO assignment of the 550 cm^{-1} M2 mode.

To summarize, the concurrent upshift of the Raman active $E(8)$ LO mode at 470 cm^{-1} and the second-order M1 modes in the Tb5 sample implies that the M1 mode should be assigned to the $E(8)$ LO mode in the $R3c$ structure. The close connection between the shape of the resonantly activated LO mode at ~620 cm^{-1} and the M3 second-order modes suggests that the M3 mode is indeed a Raman inactive A_2 LO mode in the noncentrosymmetric $R3c$ and $PbZrO_3$-type structures. Finally, a common mechanism behind the whole second-order spectra supports the $E(9)$ LO assignment of the 550 cm^{-1} M2 mode.

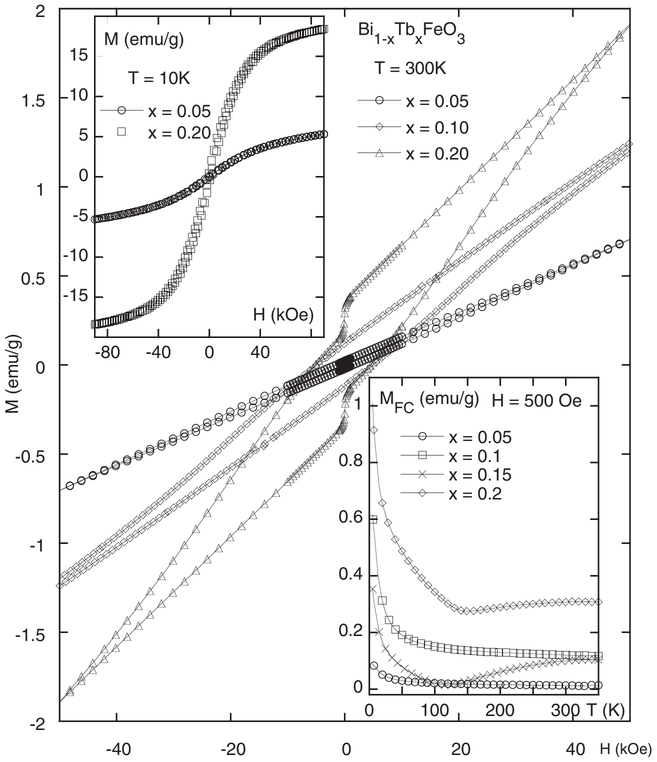

FIG. 12. Magnetization versus field at 300 K for $Bi_{1-x}Tb_xFeO_3$ with $x = 0.05$, 0.1, and 0.2. The lower right inset shows field cooled magnetization versus temperature curves for the $x = 0.05$, 0.1, 0.15, and 0.2 samples using an applied field of 500 Oe. The inset in the upper left corner shows magnetization versus field at 10 K for the $x = 0.05$ and 0.2 samples.

VI. MAGNETIC PROPERTIES

Figure 12 shows magnetization versus field curves measured at 300 K for $Bi_{1-x}Tb_xFeO_3$ with $x = 0.05$, 0.1, and 0.2. The $x = 0.05$ sample crystallizes in the $R3c$ structure and exhibits an almost linear field dependence of the magnetization in the field interval plotted in the figure. The linear dependence is expected for a sample with a cycloidally modulated antiferromagnetic structure. Measurements that were performed in the PPMS included fields up to 90 kOe and here deviation from linearity was observed for fields larger than 50 kOe (data not shown). The deviation from linearity marks the onset of a field-induced transition to a homogeneous weak ferromagnetic state. The $x = 0.1$ sample shows in comparison a larger remanent magnetization (∼0.1 emu/g) and also a larger coercive field (∼5 kOe), behavior typical of a material with a canted antiferromagnetic spin order. This is attributed to the presence of ∼30 wt.% of the orthorhombic *Pnma* structure in the sample. We note, once more, that the magnetization for the $Bi_{1-x}Tb_xFeO_3$ series was recorded on samples prepared using a solid state sintering route and this lead to a wider region of phase coexistence for the $R3c$-*Pmna* structures[15] in comparison to the samples for which Raman results are presented. The $x = 0.2$, *Pnma* sample shows a two step switching of the magnetization and similar results were also observed for the $x = 0.15$ sample that is an approximate 50:50 mixture of $R3c$ and *Pnma* phases.[15] These results are interpreted in terms of contributions from both the canted antiferromagnetic spin structure of the *Pnma* nuclear phase, and the presence of a minor terbium iron garnet (TbIG) impurity phase.[15] The existence of the TbIG impurity is hinted at by the magnetization versus temperature results shown in the lower right corner inset of Fig. 12, and was previously confirmed by XRD and neutron diffraction results.[15] The compensation temperatures, indicated in the inset by the temperature where the magnetization shows a minimum, are lower than expected for pure TbIG and comply better with results obtained for Bi substituted TbIG.[58] The magnetization versus field curve at 10 K for the $x = 0.2$ sample shows a, in comparison, strong magnetization with contributions from both the magnetism of the *Pnma* phase where the Tb^{3+} ion couples ferromagnetically to the Fe magnetic moments via a f-d exchange,[59] and the ferrimagnetically ordered garnet impurity (cf. Fig. 12, inset upper left corner).

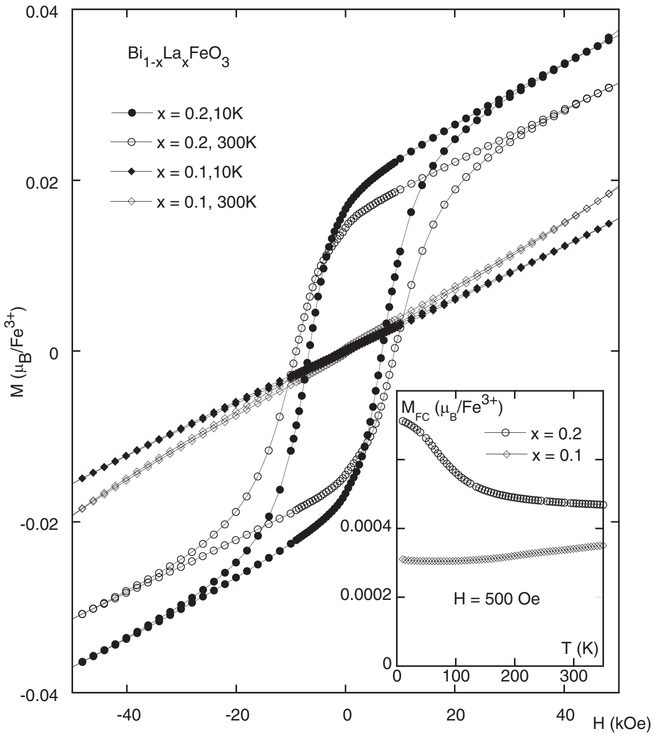

FIG. 13. Magnetization versus field at 10 and 300 K for $Bi_{1-x}La_xFeO_3$ with $x = 0.1$ and 0.2. The inset shows field cooled magnetization versus temperature curves for the same samples using an applied field of 500 Oe.

Magnetization versus field results measured at 300 and 10 K for $Bi_{1-x}La_xFeO_3$ with $x = 0.1$ and 0.2 are shown in Fig. 13. The inset shows the low field magnetization versus temperature results for the same samples. The $x = 0.1$ sample crystallizes in the $R3c$ structure and exhibits characteristics, including deviation from a linear field dependence at high fields (data not shown), typical of cycloidally modulated antiferromagnetic spin order. Our results are consistent with previous findings for $Bi_{0.9}La_{0.1}FeO_3$ that show that a weak ferromagnetic state is stabilized for fields larger than ∼100 kOe.[18,60,61] The $x = 0.2$ sample, with a structure resembling that of the antipolar $PbZrO_3$-type *Pnam* structure, exhibits a field-dependent magnetization typical of a material with a canted

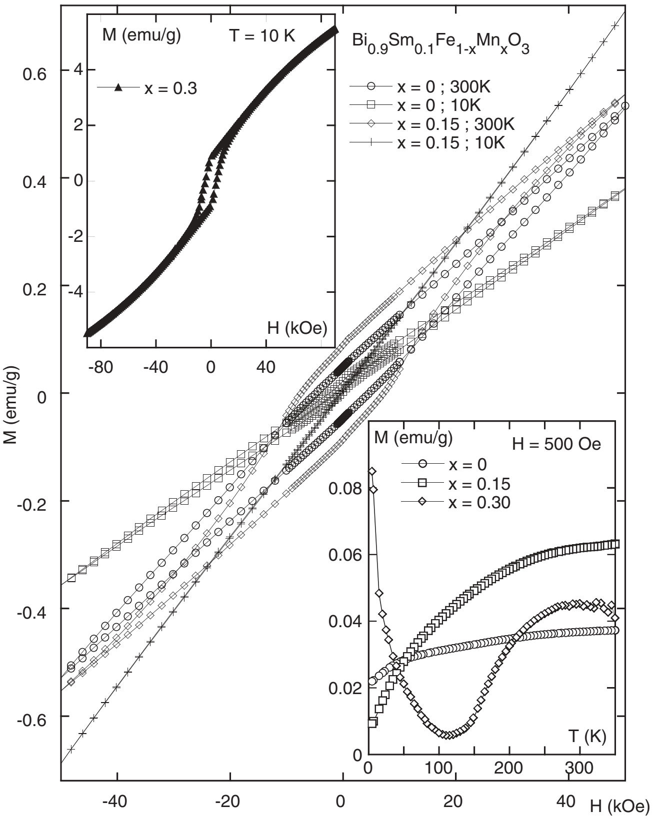

FIG. 14. Magnetization versus field at 10 and 300 K for $Bi_{0.9}Sm_{0.1}Fe_{1-x}Mn_xO_3$ with $x = 0$ and 0.15. The lower right inset shows field cooled magnetization versus temperature curves for the $x = 0$, 0.15, and 0.3 samples using an applied field of 500 Oe. The inset in the upper left corner shows magnetization versus field at 10 K for the $x = 0.3$ sample.

antiferromagnetic spin order; assuming a room temperature Fe^{3+} magnetic moment of 3.9 μ_B,[62] the observed remanent magnetization corresponds to a canting angle of $\sim 0.2^\circ$. The coercive field is close to 9 kOe at 300 K, but decreases slightly with decreasing temperature; at 10 K the coercive field has decreased to $\sim$6.5 kOe. The temperature dependence of the remanent magnetizations is the opposite; the remanent magnetization increases slightly with decreasing temperature. The evolution of the magnetic state with increasing La content observed here is similar to that reported by Rusakov *et al.*[16]

Figure 14 shows magnetization versus field curves measured at 300 and 10 K for $Bi_{0.9}Sm_{0.1}Fe_{1-x}Mn_xO_3$ with $x = 0$ and 0.15. Both samples show similar field dependence of the magnetization at 300 K; the remanent magnetization is approximately 0.05 and 0.10 emu/g for the $x = 0$ and 0.15 samples, respectively, and both samples exhibit sizable coercive fields. Thus, even if the $x = 0$ sample remains in the $R3c$ structure, it seems that the cycloidally modulated antiferromagnetic structure has at least partly been destroyed by substituting the A site with the smaller Sm^{3+} ion. Similar results for the magnetization were obtained by Khomchenko *et al.*,[22] who described the magnetic state at room temperature as a mixed antiferromagnetic/weak ferromagnetic state. The magnetization versus field measured at 10 K is even more unexpected since for both samples the hysteresis curve closes. A close to linear field dependence is observed, which is particularly striking for the biphasic (approximately 70 wt.% $R3c$: 30 wt.% $Imma$[21]) $x = 0.15$ sample, indicating a more clean, less canted, antiferromagnetic spin order and maybe even a restored cycloidally modulated antiferromagnetic structure. Additionally, this possibly suggests a low temperature structural phase transition ($T < 80$ K) of the minority $Imma$ portion of the $x = 0.15$ sample to $R3c$ symmetry, however, further measurements are required to confirm this. The inset in the lower right corner of Fig. 14 shows the temperature dependence of the low field magnetization of these two samples together with the result for the $x = 0.3$ sample. The temperature-dependent magnetization for the $x = 0.3$ sample is typical of a ferrimagnetically spin ordered sample with a compensation temperature close to the temperature where the magnetization shows a minimum. This suspicion was corroborated by close examination of the previously published neutron diffraction data[21] that showed traces of a $Sm_3Fe_5O_{12}$ garnet impurity phase. The magnetization versus field curve measured at 10 K (cf. Fig. 14, inset upper left corner) is also dominated by the strong magnetization of the ferrimagnetically ordered impurity similar to the results obtained for the $Bi_{1-x}Tb_xFeO_3$, $x = 0.15$ and 0.20 samples.

VII. SUMMARY

In summary, we have presented Raman spectra on $Bi_{1-x}Tb_xFeO_3$, $Bi_{1-x}La_xFeO_3$, and $Bi_{0.9}Sm_{0.1}Fe_{1-x}Mn_xO_3$ over a wide range of substitutions x. The structural transitions observed in the Raman spectra are in good agreement with the XRD data and previously published neutron diffraction data[15,16,21] and the observed structures are collected in Table I.

The large ionic radii mismatch on the A site in $Bi_{1-x}Tb_xFeO_3$ induces a single transition from $R3c$ to $Pnma$ of the $GdFeO_3$ type at $x = 0.175$, although a phase coexistence is observed already at $x = 0.125$. $Bi_{1-x}La_xFeO_3$ is found to undergo a more complicated transition from ferroelectric $R3c$ to an antiferroelectric $PbZrO_3$ structure at $x = 0.2$, with signs of phase mixture at $x = 0.15$ and 0.175. The antiferroelectric structure is maintained up to $x = 0.4$, after which the final

TABLE I. Summary of the observed space groups based on a combination of the Raman and XRD results. The $PbZrO_3$-type structure is discussed in Sec. V C.

$Bi_{1-x}Tb_xFeO_3$	
$0 \leqslant x \leqslant 0.1$	$R3c$
$0.125 \leqslant x \leqslant 0.15$	$R3c + Pnma$
$0.175 \leqslant x \leqslant 1$	$Pnma$
$Bi_{1-x}La_xFeO_3$	
$0 \leqslant x \leqslant 0.1$	$R3c$
$0.15 \leqslant x \leqslant 0.175$	$R3c + PbZrO_3$ type
$0.2 \leqslant x \leqslant 0.4$	$PbZrO_3$ type
$0.5 \leqslant x \leqslant 1$	$Pnma$
$Bi_{0.9}Sm_{0.1}Fe_{1-x}Mn_xO_3$	
$x = 0$	$R3c$
$x = 0.15$	$R3c + Imma$
$x = 0.3$	$Imma$

Pnma structure of the end-member $LaFeO_3$ is obtained. The *A*- and *B*-site substituted $Bi_{0.9}Sm_{0.1}Fe_{1-x}Mn_xO_3$ series transforms instead from $R3c$ to *Imma*, starting at $x = 0.15$. We interpret the conflicting results between our results and those in Ref. 22 as a sign of a large sensitivity in these materials to the exact condition during the synthesis.

The spectra of the $R3c$ phase samples reveals a pseudosoft behavior of the 220 cm^{-1} mode, thus implying an A_1 assignment of this mode that correlates the Raman shift with the degree of octahedral tilt due to a combination of lone-pair dilution and ionic-size differences on the *A* site. This lends support to the first-principle calculations by Hermet *et al.*[42] and the phonon assignments by Hlinka *et al.*[33] Away from the $R3c$ phase, a comparison between the *Pnma* structures in La and Tb substituted samples allows us to assign the broad bands observed in the Raman spectra in these substitution series.

With the help of Raman spectra of both the $Bi_{1-x}Tb_xFeO_3$ and $Bi_{1-x}La_xFeO_3$ series as well as the end-members $BiFeO_3$ and $LaFeO_3$, a detailed analysis of the strong second-order Raman scattering is presented, where the first- and second-order modes are assigned to LO modes and their Fröhlich-interaction enhanced second-order scattering, respectively. In the $R3c$ structures, the LO mode at ~620 cm^{-1} is found to be a Raman inactive A_2 mode with a strong resonant enhancement in all *A*-site substituted samples, while the 470 and 550 cm^{-1} modes belong to the dipole-allowed Raman active LO modes.

The recorded magnetization is consistent with a cycloidally modulated antiferromagnetic arrangement of the Fe spins in the $R3c$ structures. Upon increasing *A*-site substitution a transition towards a canted antiferromagnetic spin structure is observed, coincident with the structural transition away from $R3c$. In contrast, the $Bi_{0.9}Sm_{0.1}Fe_{1-x}Mn_xO_3$ series shows an anomalous closing of the hysteresis loop at 10 K, indicating a reversal to a noncanted, perhaps cycloidally modulated, antiferromagnetic state at low temperatures. The transition from cycloidally modulated spins to a canted collinear antiferromagnetic ordering is possibly seen also in the intensity decrease of the Fe derived vibrational modes as the degree of substitution is increased.

Further investigations are needed to understand the anomalous low temperature behavior of $Bi_{0.9}Sm_{0.1}Fe_{1-x}Mn_xO_3$, $x = 0$–0.15, as well as the connection between *A*-site substitution and spin structure in the ferroelectric $R3c$ phases.

ACKNOWLEDGMENTS

C.S.K. acknowledges support from the Swedish research council (Vetenskapsrådet) Grant No. 621-2011-3851.

---

[*] johan.bielecki@chalmers.se

[1] T. Zhao, A. Scholl, F. Zavliche, K. Lee, M. Barry, A. Doran, M. P. Cruz, Y. H. Chu, C. Ederer, N. A. Spaldin, R. R. Das, D. M. Kim, S. H. Baek, C. B. Eim, and R. Ramesh, Nat. Mater. **5**, 823 (2006).

[2] G. Catalan and J. F. Scott, Adv. Mater. **21**, 2463 (2009).

[3] W. Eerenstein, N. D. Mathur, and J. F. Scott, Nature (London) **442**, 759 (2006).

[4] J. Wang, J. B. Nheaton, H. Zheng, V. Nagarajan, S. B. Ogale, B. Liu, D. Viehland, V. Vaithyanathan, D. G. Schlom, U. V. Waghmare, N. A. Spaldin, K. M. Rabe, M. Wuttig, and R. Ramesh, Science **299**, 1719 (2003).

[5] S.-T. Zhang, Y. Zhang, M.-H. Lu, C.-L. Du, Y.-F. Cheng, Z.-G. Liu, Y.-Y. Zhu, N.-B. Ming, and X. Q. Pan, Appl. Phys. Lett. **88**, 162901 (2006).

[6] G. L. Yuan, K. Z. Baba-Kishi, J.-M. Lium, S. W. Or, Y. P. Wang, and Z. G. Liu, J. Am. Ceram. Soc. **89**, 3136 (2006).

[7] I. Sosnowska, W. Schafer, W. Kockelmann, K. H. Andersen, and I. O. Troyanchuk, Appl. Phys. A **74**, 1040 (2002).

[8] A. M. Glazer, Acta Crystallogr. Sect. B **28**, 3384 (1972).

[9] P. Ravindran, R. Vidya, A. Kjekshus, H. Fjellvåg, and O. Eriksson, Phys. Rev. B **74**, 224412 (2006).

[10] I. Sosnowska, T. Peterlin-Neumaier, and E. Steichele, J. Phys. C **15**, 4835 (1982).

[11] C. Ederer and N. A. Spaldin, Phys. Rev. B **71**, 060401(R) (2005).

[12] D. Lebeugle, D. Colson, A. Forget, M. Viret, A. M. Bataille, and A. Goukasov, Phys. Rev. Lett. **100**, 227602 (2008).

[13] R. D. Shannon, Acta Crystallogr. Sect. A **32**, 751 (1976).

[14] Here we use values for the ionic radii corresponding to an eightfold coordination.

[15] S. Saxin and C. S. Knee, J. Solid State Chem. **184**, 1576 (2011).

[16] D. A. Rusakov, A. M. Abakumov, K. Yamaura, A. A. Belik, G. Van Tendeloo, and T.-M. Eiji, Chem. Mater. **23**, 285 (2011).

[17] S. Karimi, I. M. Reaney, Y. Han, J. Pokorny, and I. Sterianou, J. Mater. Sci. **44**, 5102 (2009).

[18] I. O. Troyanchuk, M. V. Bushinsky, D. V. Karpinsky, O. S. Mantytskaya, V. V. Fedotova, and O. I. Prochnenko, Phys. Status Solidi B **246**, 1901 (2009).

[19] I. O. Troyanchuk, D. V. Karpinsky, M. V. Bushinsky, V. A. Khomchenko, G. N. Kakazei, J. P. Araujo, M. Tovar, V. Sikolenko, V. Efimov, and A. L. Kholkin, Phys. Rev. B **83**, 054109 (2011).

[20] H. Fujishita, Y. Shiozaki, N. Achiwa, and E. Sawaguchi, J. Phys. Soc. Jpn. **51**, 3583 (1982).

[21] S. Saxin and C. S. Knee, Dalton Trans. **40**, 3462 (2011).

[22] V. A. Khomchenko, I. O. Troyanchuk, M. I. Kovetskaya, and J. A. Paixão, J. Appl. Phys. **11**, 014110 (2012).

[23] C. Beekman, A. A. Reijnders, Y. S. Oh, S. W. Cheong, and K. S. Burch, Phys. Rev. B **86**, 020403(R) (2012).

[24] H. Fukumura, H. Harima, K. Kisoda, M. Tamada, Y. Noguchi, and M. Miyayama, J. Magn. Magn. Mater. **310**, e367 (2006).

[25] R. Palai, J. F. Scott, and R. S. Katiyar, Phys. Rev. B **81**, 024115 (2010).

[26] M. O. Ramirez *et al.*, Appl. Phys. Lett. **94**, 161905 (2009).

[27] M. O. Ramirez, M. Krishnamurthi, S. A. Denev, A. Kumar, S.-Y. Yang, Y. H. Chu, E. Saiz, J. Seidel, A. P. Pyatakov, A. Bush, D. Viehland, J. Orenstein, R. Ramesh, and V. Gopalan, Appl. Phys. Lett. **92**, 022511 (2008).

[28] P. Rovillain, M. Cazayous, Y. Gallais, A. Sacuto, R. P. S. M. Lobo, D. Lebeugle, and D. Colson, Phys. Rev. B **79**, 180411(R) (2009).

[29] R. Haumont, J. Kreisel, P. Bouvier, and F. Hippert, Phys. Rev. B **73**, 132101 (2006).

[30] Y. Yang, J. Y. Sun, K. Zhu, Y. L. Liu, J. Chen, and X. R. Xing, Physica B **404**, 171 (2009).

[31] M. G. Guennou, P. Bouvier, G. S. Chen, B. Dkhil, R. Haumont, G. G. Garbarino, and J. Kreisel, Phys. Rev. B **84**, 174107 (2011).

[32] R. Palai, H. Schmid, J. F. Scott, and R. S. Katiyar, Phys. Rev. B **81**, 064110 (2010).

[33] J. Hlinka, J. Pokorny, S. Karimi, and I. M. Reaney, Phys. Rev. B **83**, 020101(R) (2011).

[34] J. Andreasson, J. Holmlund, R. Rauer, M. Käll, L. Börjesson, C. S. Knee, A. K. Eriksson, S.-G. Eriksson, M. Rübhausen, and R. P. Chaudhury, Phys. Rev. B **78**, 235103 (2008).

[35] J. Andreasson, J. Holmlund, C. S. Knee, M. Käll, L. Börjesson, S. Naler, J. Bäckström, M. Rübhausen, A. K. Azad, and S.-G. Eriksson, Phys. Rev. B **75**, 104302 (2007).

[36] Y. Yang, Y.-L. Liu, K. Zhu, L.-Y. Zhang, L.-Y. Zhang, J. Liu, and Y.-J. Jiang, Chin. Phys. B **19**, 037802 (2010).

[37] H. M. Rietveld, Appl. Crystallogr. **2**, 65 (1969).

[38] A. C. Larson and R. B. von Dreele, Generalised Structure Analysis System Report LAUR86-748, Los Alamos National Laboratory, 2004.

[39] E. Kroumova, M. I. Aroyo, J. M. Perez-Mato, A. Kirov, C. Capillas, S. Ivantchev, and H. Wondratschek, Phase Transitions **76**, 155 (2003).

[40] M. N. Iliev, A. P. Litvinchuk, V. G. Hadjiev, Y.-Q. Wang, J. Cmaidalka, R.-L. Meng, Y.-Y. Sun, N. Kolev, and M. V. Abrashev, Phys. Rev. B **74**, 214301 (2006).

[41] A. A. Porporati, K. Tsuji, M. Valant, A.-K. Axelsson, and G. Pezzotti, J. Raman Spectrosc. **41**, 84 (2010).

[42] P. Hermet, M. Goffinet, J. Kreisel, and Ph. Ghosez, Phys. Rev. B **75**, 220102(R) (2007).

[43] J. Andreasson, J. Holmlund, S. G. Singer, C. S. Knee, R. Rauer, B. Schulz, M. Käll, M. Rübhausen, S.-G. Eriksson, L. Börjesson, and A. Lichtenstein, Phys. Rev. B **80**, 075103 (2009).

[44] M. Reedyk, C. Thomsen, M. Cardona, J. S. Xue, and J. E. Greedan, Phys. Rev. B **50**, 13762 (1994).

[45] M. V. Abrashev, A. P. Litvinchuk, C. Thomsen, and V. N. Popov, Phys. Rev. B **55**, R8638 (1997).

[46] M. Cardona, in *Topics in Applied Physics (Light Scattering in Solids II)*, edited by M. Cardona and G. Güntherodt, Vol. 50 (Springer, Berlin, 1982), pp. 128–135.

[47] N. D. Todorov, M. V. Abrashev, and V. G. Ivanov, J. Phys.: Condens. Matter **24**, 175404 (2012).

[48] M. Goffinet, P. Hermet, D. I. Bilc, and Ph. Ghosez, Phys. Rev. B **79**, 014403 (2009).

[49] A. Palewicz, I. Sosnowska, R. Przeniosło, and A. W. Hewat, Acta Phys. Pol. A **117**, 296 (2010).

[50] W. Hayes and R. Loudon, *Scattering of Light by Crystals* (John Wiley, New York, 1978).

[51] M. Kubota, K. Oka, Y. Nakamura, H. Yabuta, K. Miura, Y. Shimakawa, and M. Azuma, Jpn. J. Appl. Phys. **50**, 09NE08 (2011).

[52] A. E. Pasto and R. A. Condrate, J. Am. Ceram. Soc. **56**, 436 (1973).

[53] M. N. Iliev, M. V. Abrashev, H.-G. Lee, V. N. Popov, Y. Y. Sun, C. Thomsen, R.-L. Meng, and C. W. Chu, Phys. Rev. B **57**, 2872 (1998).

[54] M. V. Abrashev, J. Backstrom, L. Borjesson, V. N. Popov, R. A. Chakalov, N. Kolev, R.-L. Meng, and M. N. Iliev, Phys. Rev. B **65**, 184301 (2002).

[55] R. Ouillon, J.-P. Pinan-Lucarre, P. Ranson, Ph. Pruzan, R. Ranjan, and D. Pandey, J. Phys.: Condens. Matter **14**, 2079 (2002).

[56] An early analysis of the second-order spectrum in BFO was presented in Ref. 27. That mode assignment is however not consistent with recent, more detailed, phonon assignments of the first-order scattering.[23,33]

[57] S. Kamba, D. Nuzhnyy, M. Savinov, J. Šebek, J. Petzelt, J. Prokleška, R. Haumont, and J. Kreisel, Phys. Rev. B **75**, 024403 (2007).

[58] M. Guilot, H. Le Gall, J. M. Desvignes, and M. Artinian, IEEE Trans. Magn. **30**, 4419 (1994).

[59] V. A. Khomchenko, V. V. Shvartsman, P. Borisov, W. Kleemann, D. A. Kiselev, I. K. Bdkin, J. M. Vieira, and A. L. Kholkin, Acta Mater. **57**, 5137 (2009).

[60] G. Le Bras, D. Colson, A. Forget, N. Genand-Riondet, R. Tourbot, and P. Bonville, Phys. Rev. B **80**, 134417 (2009).

[61] G. le Bras, P. Bonville, D. Colson, A. Forget, N. Genand-Rionet, and R. Tourbot, Physica B **406**, 1492 (2011).

[62] A. Palewicz, R. Przeniosłom, I. Sosnowska, and A. W. Hewat, Acta Crystallogr. Sect. B **63**, 537 (2007).